

Theory of intervalley-coherent AFM order and topological superconductivity in tWSe₂

Ammon Fischer,^{1,*} Lennart Klebl,^{2,3} Valentin Crépel,⁴ Siheon Ryee,³ Angel Rubio,^{5,6} Ledo Xian,^{7,8,5} Tim O. Wehling,^{3,9} Antoine Georges,^{10,4,11,12} Dante M. Kennes,^{1,5} and Andrew J. Millis^{4,13}

¹*Institute for Theory of Statistical Physics, RWTH Aachen University, and JARA Fundamentals of Future Information Technology, 52062 Aachen, Germany*

²*Institute for Theoretical Physics and Astrophysics and Würzburg-Dresden Cluster of Excellence ct.qmat, University of Würzburg, 97074 Würzburg, Germany*

³*I. Institute of Theoretical Physics, Universität Hamburg, Notkestraße 9-11, 22607 Hamburg, Germany*

⁴*Center for Computational Quantum Physics, Flatiron Institute, New York, NY 10010, USA*

⁵*Max Planck Institute for the Structure and Dynamics of Matter, Center for Free Electron Laser Science, 22761 Hamburg, Germany*

⁶*Center for Computational Quantum Physics, Simons Foundation Flatiron Institute, New York, NY 10010 USA*

⁷*Tsientang Institute for Advanced Study, Zhejiang 310024, China*

⁸*Songshan Lake Materials Laboratory, 523808 Dongguan, Guangdong, China*

⁹*The Hamburg Centre for Ultrafast Imaging, 22761 Hamburg, Germany*

¹⁰*Collège de France, 11 place Marcelin Berthelot, 75005 Paris, France*

¹¹*CPHT, CNRS, Ecole Polytechnique, Institut Polytechnique de Paris, Route de Saclay, 91128 Palaiseau, France*

¹²*DQMP, Université de Genève, 24 quai Ernest Ansermet, CH-1211 Genève, Suisse*

¹³*Department of Physics, Columbia University, 538 West 120th Street, New York, NY 10027, USA*

The recent observation of superconductivity in the vicinity of insulating or Fermi surface reconstructed metallic states has established twisted bilayers of WSe₂ as an exciting platform to study the interplay of strong electron-electron interactions, broken symmetries and topology. In this work, we study the emergence of electronic ordering in twisted WSe₂ driven by gate-screened Coulomb interactions. Our first-principles treatment begins by constructing moiré Wannier orbitals that faithfully capture the bandstructure and topology of the system and project the gate-screened Coulomb interaction onto them. Using unbiased functional renormalization group calculations, we find an interplay between intervalley-coherent antiferromagnetic order and chiral, mixed-parity d/p -wave superconductivity for carrier concentrations near the displacement field-tunable van-Hove singularity. Our microscopic approach establishes incommensurate intervalley-coherent antiferromagnetic spin fluctuations as the dominant electronic mechanism driving the formation of superconductivity in $\theta = 5.08^\circ$ twisted WSe₂ and demonstrates that nesting properties of the Fermi surface sheets near the higher-order van-Hove point cause an asymmetric density dependence of the spin ordering as the density is varied across the van-Hove line, in good agreement with experimental observations. We show how the region of superconducting and magnetic order evolves within the two-dimensional phase space of displacement field and electronic density as twist angle is varied between $4^\circ \dots 5^\circ$.

I. INTRODUCTION

Transition metal dichalcogenide (TMD) heterostructures have arisen as fertile and highly versatile platforms for exploring the interplay between topology and strong electronic correlations [1], hosting correlated insulators [2–4], spin-ordered metals [5–7], rich multi-orbital physics [8, 9], Feschbach resonances [10–16], quantum critical behavior [17, 18], excitonic insulators [19–22], topological Kondo physics [23–28], quantum anomalous and quantum spin-Hall insulators [29, 30], ferromagnetic fractional quantum anomalous phases [31–34], or gapped spin liquids [35, 36]. Additionally, early experiments on 5.0° twisted WSe₂ hinted at the existence of superconducting phases in moiré TMDs [2]; a finding recently confirmed by sub-Kelvin transport measurements on 3.65° [37] and 5.1° [38] twisted samples. The discovery of superconductivity in these highly tunable moiré TMDs has sparked many theoretical studies [39–49] for the new

insights it promises to provide on the origin and properties of strongly correlated topological superconductivity, including exciting prospects for trapping non-abelian anyons at clean, gate-defined interfaces [50–53].

Twisted WSe₂ (tWSe₂) consists of two WSe₂ layers stacked at a relative twist angle θ which are encapsulated in a structure including top and bottom gates. The twist, in combination with the electrostatic potential from the local arrangement of WSe₂ bilayers and the interlayer electronic hybridization, produces a large unit cell with two dimensional “moiré” bands [54, 55]. The average of the potentials on the top and bottom gates tunes the electronic density over wide ranges. The difference in voltage between the top and bottom gates introduces an interlayer potential difference, or “displacement field”, which shifts electronic wave functions and charge density between the layers, modifying the electronic band structure. At a fixed twist angle, the system’s behavior can be explored in a phase diagram defined by electronic density and displacement field. As the density varies at a fixed displacement field, the Fermi surface can pass through a van-Hove singularity (VHS), where the density of states

* ammon.fischer@rwth-aachen.de

diverges. Of particular relevance for this study is that both the density at which a van-Hove singularity occurs and the strength of the resulting divergence in the density of states depend on twist angle and are tunable over wide ranges by varying the displacement field.

In the 5.1° tWSe₂ device [38], the superconducting state is observed only for a small range of displacement fields near the hole density n/n_0 at which the Fermi surface passes through the van-Hove singularity, and is adjacent to a metallic region characterized by an increase in longitudinal resistance and a very rapid non-monotonic doping dependence of the Hall resistivity. This unusual metallic region has been interpreted [38] as arising from the emergence of antiferromagnetic (AFM) spin ordering that partially gaps out the Fermi surface. The densities at which superconductivity and antiferromagnetism occur are not close to one hole per moiré unit cell and the experimentally important displacement fields are significant, on the order of half of the field required to fully layer-polarize the doped holes. In the 3.65° device [37], superconductivity is found only for carrier concentrations near $n/n_0 = 1$ per moiré unit cell as well as small displacement fields, with the superconductivity giving way to an insulating phase and then to an apparently conventional metallic phase as the displacement field is increased. In each device, the superconducting and AFM or insulating states are found only in a relatively small region of the experimental phase space defined by carrier concentration and interlayer (displacement field) potential difference.

The association of superconductivity with proximity to the non-integer carrier concentration at which the Fermi surface contains the VHS, and the proximity to an apparent metallic antiferromagnetic phase suggests a weak-to-moderate coupling scenario in the 5.1° device, where the effects of electron-electron interactions are amplified by the density of states divergence associated with the van-Hove point. The association of superconductivity at particular values of the displacement field may then be related to proximity to a higher order van-Hove singularity (HOVHS) with a stronger density of states divergence appearing as the band theory is tuned [56]. Recent literature has presented various versions of this scenario. Interactions considered include spin-fluctuations [39, 41, 47], over-screened Coulomb interactions [45] and phenomenological attraction [43, 46]. While these treatments provide important insights, they are based on particular *ansätze* and come to different conclusions regarding the symmetry of the superconducting state.

Moreover, theory should take into account the non-trivial topological properties [55, 57, 58] of the low-lying hole bands. In addition to potentially endowing the superconducting state with interesting properties [45], they obstruct an effective single-orbital description of the top-most moiré valence band and imply that interactions projected onto the top-most band generically have a long-ranged structure. A minimal faithful low-energy model of tWSe₂ comprises three orbitals per valley that are cen-

tered on the triangular and honeycomb sites of the moiré superlattice [57, 59]. Such a model accurately accounts for the topological entanglement of the topmost valence bands with Bloch states far below the Fermi energy and for the subtle aspects of the fermiology and its dependence on the displacement field. In this multi-orbital Wannier basis, the gate-screened Coulomb interactions relevant for the experimental setup can be cast into fairly local interactions, which ensures the applicability of established many-body techniques beyond the mean-field level [45, 46], including the functional renormalization group [60–64] (FRG), dynamical mean-field theory [65], or tensor network based approaches [66, 67]. A similar situation arises in twisted bilayers of graphene, where a multi-band “heavy fermion” description is argued to best represent the physics [68, 69].

In this work, we go beyond initial phenomenological treatments of correlated phases in tWSe₂ and provide a full-fledged analysis of correlated states in the weak-to-moderate interaction regime based on physically realistic repulsive gate-screened Coulomb interactions projected onto a multiband model based on exponentially localized Wannier functions that captures the topology and the intricacies of the band structure. Using unbiased functional renormalization group techniques, we map out the interacting phase diagram of tWSe₂ in the twist angle range $\theta = 4^\circ \dots 5^\circ$ from *first principles*. We demonstrate that intervalley-coherent anti-ferromagnetic (IVC-AFM) order and extended regions of chiral d/p -wave superconductivity coexist along the gate-tunable van-Hove line. The unbiased characterization of particle-hole and particle-particle instabilities in conjunction with the subtle fermiology near the van-Hove line enabled by our choice of methods permits us to show that the electronic driving mechanism for superconductivity in tWSe₂ is primarily facilitated by spin fluctuations around regions of incommensurate IVC-AFM order below the higher order van-Hove singularity, where the absence of perfect nesting strengthens particle-particle fluctuations. Our microscopic approach can explain several features observed in recent experimental measurements, including the unusual density dependence of the particle-hole instabilities with respect to the van-Hove line. We predict a successive shift of superconducting regions to lower values of the displacement field and towards $n/n_0 \sim 1$ as the twist angle is decreased and briefly discuss the connection of our results to observations on the $\theta = 3.65^\circ$ sample, where superconductivity is observed for $n/n_0 \sim 1$ and for small displacement fields.

II. MODEL AND METHOD

A. Multi-orbital Wannier model

The non-interacting electronic structure of hole-doped tWSe₂ is accurately described by a continuum model in which the spin-valley locked holes of both monolayers

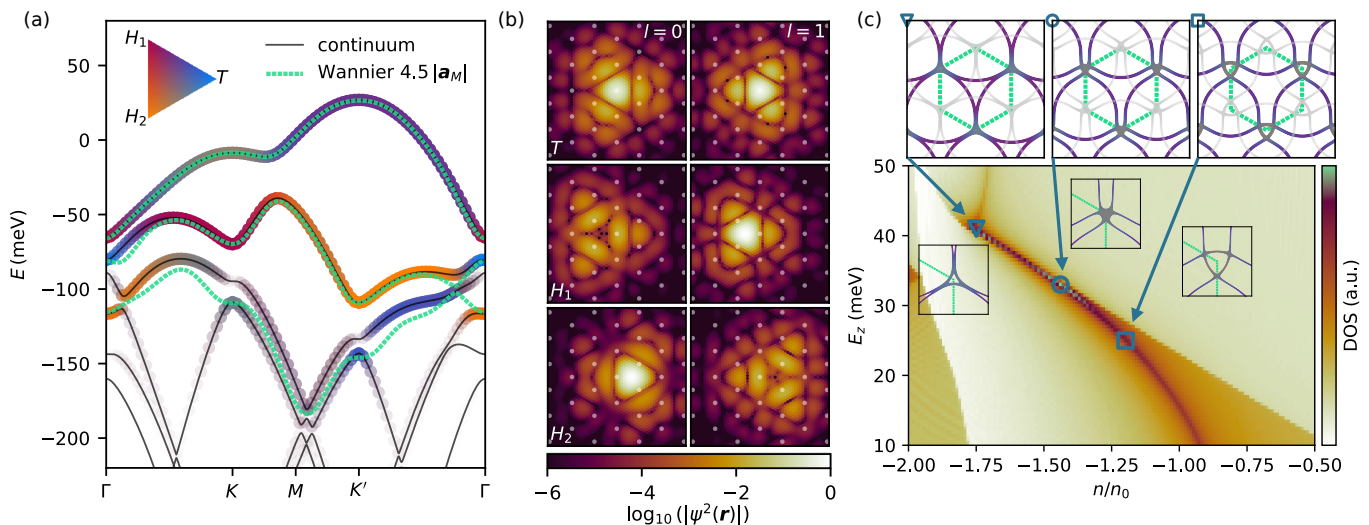


FIG. 1. Fermiology and Wannierization of $\theta = 5.08^\circ$ tWSe₂ for an external displacement field $E_z = 20$ meV. (a) Continuum bandstructure in valley $\nu = +1$ (black) and spectral overlap of its Bloch states with a three-orbital model comprising Wannier orbitals centered at the triangular (T , s -orbital) and honeycomb (H_1 , p_+ -orbital)/(H_2 , p_+ -orbital) sites of the moiré superlattice (tri-colored map). The bandstructure of the effective Wannier model truncated after 4.5 moiré lattice vectors is indicated by the green dashed line. (b) Amplitude $|\psi_l(\mathbf{r})|^2$ of the Wannier functions (T , H_1 , H_2) on the two layers ($l = 0, 1$) that capture the spectral weight of the continuum model. (c) Density of states as function of holes per moiré unit cell n/n_0 and displacement field E_z . The upper panel shows snapshots of the Fermi surface along the van-Hove line and its orbital polarization using the same colormap as in (a) for valley $\nu = +1$. The Fermi surface of the opposite valley $\nu = -1$ is shown in gray. The green dashed line indicates the mini-Brillouin zone of tWSe₂. The blue circle indicates the position of the higher-order VHS, where three van-Hove points merge at K' as demonstrated in the insets. The three van-Hove points are moved towards Γ (M) for increasing (decreasing) value of the external displacement field along the van-Hove line as indicated by the blue triangle (square).

are treated within the effective mass approximation, and are coupled by moiré potentials that slowly vary on the atomic scale [54]. Due to the emergent spin-valley locking in monolayer WSe₂, the low-energy states can be assigned a well-defined valley index $\nu = \pm 1$ and states from opposite spin-valley sectors are related by virtue of time-reversal symmetry \mathcal{T} . The effects of out-of-plane electric fields are captured by a layer-dependent potential energy $\pm E_z$. For twist angles $\theta \gtrsim 3^\circ$, in-plane lattice relaxation is weak, and the associated moiré fields are characterized by only a few harmonics [70–74]. Here, we use the continuum model from Ref. [55], whose coefficients have been fitted to large-scale *ab-initio* calculations, see Supplementary Materials (SM) [75] for details.

As most many-body methods require a symmetry-preserving lattice description of the system under scrutiny, we seek to construct a Wannier representation of the topmost valence band states in each valley based on the three-orbital model put forward in Refs. [57, 59]. This model is based on generic symmetry arguments and comprises one triangular lattice site T (at Wyckoff position 1a of the triangular superlattice), which has weight on both layers, as well as two honeycomb lattice sites $H_{1,2}$ (at Wyckoff positions 2a,b) with dominant weight on either one of the layers. At a twist angle of $\theta = 5.08^\circ$, however, the Chern number sequence of the first three valence bands of tWSe₂ in valley $\nu = \pm 1$ is (ν, ν, ν) for the parameters of Ref. [55], prohibiting an exponential

localization of Wannier functions centered at aforementioned Wyckoff positions constructed from the three topmost bands alone. We resolve this issue by employing a single-shot Wannierization scheme [76–78] in which Bloch states from the entire valence band manifold are considered for the projection and a proper subspace selection is instead achieved by weighting Bloch states according to their energetic hierarchy and their weight around the desired orbital center. Compared to the layer-polarization scheme presented in Ref. [57], the energetic subspace selection ensures to construct exponentially localized Wannier functions irrespective of the Chern number of the third moiré band, which sensitively depends on model parameters due to the large energy overlap of this band with remote energy bands. Figure 1 (a) shows the band structure of the Wannier model (dashed cyan lines) compared to the continuum model (black lines) at a displacement field $E_z = 20$ meV. By adding the overlap of each Wannier function with the continuum model’s Bloch states as color, we demonstrate how states from the fourth and fifth bands are essential for a three-orbital description with an overall Chern number sequence $(\nu, \nu, -2\nu)$. The residual spectral weight in remote energy bands is required to render the entire Wannier band manifold topologically trivial. In spite of this, the topmost band of the continuum model is perfectly reproduced in the Wannier model as shown in Fig. 1 (a).

In accordance with previous studies, the topmost band

has significant weight in the T -orbital [2, 9, 41, 79–84], but the nontrivial topology invalidates a description as a one-band model. This contrasts MoTe₂ bilayers [57, 59] in which more weight lies in the $H_{1,2}$ orbitals, leading to different physical behaviors. In Fig. 1 (b), we display the real-space structure of the three Wannier orbitals. Their exponential localization implies short-ranged hopping parameters as demonstrated in Fig. 1 (a): Disregarding hopping parameters for distances $d \gtrsim 4.5 |\mathbf{a}_M|$ (with \mathbf{a}_M the moiré lattice vectors) does not change the resulting band structure significantly. A detailed analysis of the energetic and topological properties of the Wannier functions is provided in the SM [75]. We carry out the Wannierization for several values of displacement field E_z and interpolate the hopping parameters in order to obtain a Hamiltonian for arbitrary E_z . The resulting density of states is a smooth function of E_z [see Fig. 1 (c)], and displays a clear maximum when the Fermi energy meets the VHS of the topmost valence band [39]. Along this line, an exceptional point occurs at $E_z \approx 33$ meV (blue circle), where three van-Hove points merge with each other and form a HOVHS [56]. For $E_z < E_z^c$, the three van-Hove points move towards the M -point forming small triangular Fermi pockets around K^ν that are exclusively T/H_2 -polarized. In contrast, for $E_z > E_z^c$, the three van-Hove points move towards Γ , and the Fermi pockets around K^ν disappear. The remaining dispersive part of the Fermi surface is entirely T/H_2 -polarized for all values of the displacement field. The multi-orbital Wannier model has the symmetry group $\mathcal{G}_0 = C_{3z} \otimes U_\nu(1) \otimes \mathcal{T}$, where C_{3z} is the point group of the moiré unit cell that contains a three-fold rotation around the z -axis, the $U_\nu(1)$ -symmetry acts in spin-valley space and \mathcal{T} denotes time-reversal symmetry. Due to the absence of cubic terms to lowest order in the continuum description [57], the system we study theoretically further possesses a mirror-symmetry in each valley \mathcal{M}_x that is weakly broken in the physical bilayer but is visible in the fermiology of a single spin-valley sector in Fig. 1 (c).

With the tight-binding Wannier model for arbitrary E_z as well as interaction parameters from projection of the dual-gated Coulomb interaction onto the Wannier functions (see SM [75]) at hand, we can formulate the interacting low-energy Hamiltonian as

$$H = \sum_{\nu, \mathbf{R}, \mathbf{R}'} \sum_{X, X'} t_{\mathbf{R}X, \mathbf{R}'X'}^\nu c_{\mathbf{R}X}^{\nu\dagger} c_{\mathbf{R}'X'}^\nu + \sum_{\nu, \mathbf{R}} \sum_{X \in \{T, H_1, H_2\}} \frac{U_X}{2} n_{\mathbf{R}X}^\nu n_{\mathbf{R}X}^{\bar{\nu}}, \quad (1)$$

where ν denotes the locked spin-valley degree of freedom, X, X' orbital, and \mathbf{R}, \mathbf{R}' Bravais lattice vectors. The operator $c_{\mathbf{R}X}^{\nu(\dagger)}$ destroys (creates) an electron with spin/valley ν in the orbital X on site \mathbf{R} , and $n_{\mathbf{R}X}^\nu = c_{\mathbf{R}X}^{\nu\dagger} c_{\mathbf{R}X}^\nu$ is the density operator. As the hopping parameters $t_{\mathbf{R}X, \mathbf{R}'X'}^\nu$ are valley-diagonal, the interaction part is what couples different spins/valleys. To disentangle the microscopic mechanisms responsible for the for-

mation of the Fermi surface reconstructed AFM phase and superconductivity observed in experimental measurements [37, 38], we first consider the dominant on-site interaction associated to the triangular (U_T) and honeycomb ($U_{H_{1,2}}$) sites and later investigate the influence of long-ranged density-density interaction on the phase diagram of $\theta = 5.08^\circ$ tWSe₂. The values of $U_T \approx 74$ meV and $U_H \approx 106$ meV place tWSe₂ into the weak-to-intermediate coupling regime, where the bandwidth $W \approx 200$ meV of the three-orbital model fulfills $W \gtrsim U_{T/H}$. We note that due to the topological entanglement of the topmost valence bands in tWSe₂, the bandwidth of the entire Wannier band manifold (and not only the topmost valence band) should be considered.

B. Functional renormalization group approach

In the weak-to-moderate coupling regime, the functional renormalization group (FRG) [60–64] represents a well-established method to predict particle-particle and particle-hole instabilities in an unbiased manner. FRG smoothly connects the non-interacting action to the interacting one by virtue of a renormalization group (RG) scale $\Lambda = \infty \rightarrow 0$. The introduction of the RG scale leads to an infinite hierarchy of coupled differential equations for the vertex functions $\Gamma^{(2n)}$. In order to numerically solve the coupled nonlinear functional differential equations, we must truncate the hierarchy and approximate the vertex functions' dependencies on frequency and momentum. To account for the topology of the multi-orbital Wannier setup for the moiré valence bands, we here employ the static four-point truncated unity FRG (TUFRG) approximation [85–87] that allows to keep track of the entire orbital/band and (incommensurate) momentum dependence of the model at the expense of neglecting the frequency dependence of the vertex functions. Most importantly, this allows to treat all couplings on equal footing and (at one loop order) accounts for mutual feedback between the different interaction channels that are renormalized during the flow. The vertex functions are parametrized in a hybrid real-momentum space representation [87, 88] using a 30×30 momentum mesh for the bosonic momentum variable in each two-particle reducible interaction channel—hence allowing to resolve (in)commensurate particle-particle and particle-hole instabilities—whereas the fermionic momenta are expanded in a real-space form factor basis that is truncated after a distance of $2|\mathbf{a}_M|$. The propagator is resolved on a refined 900×900 momentum mesh to increase the energy resolution and to sufficiently resolve the fermiology of the system at low scales, see SM [75] for details. In static four-point (TU)FRG, the onset of an ordered phase is signaled by the divergence of the two-particle vertex $\Gamma^{(4)}$ at a particular (critical) scale Λ_c . The most divergent eigenvalue (and the accompanying eigenvector) of $\Gamma^{(4)}$ then provides insights into the structure of the ordered phase—whether it is a particle-particle

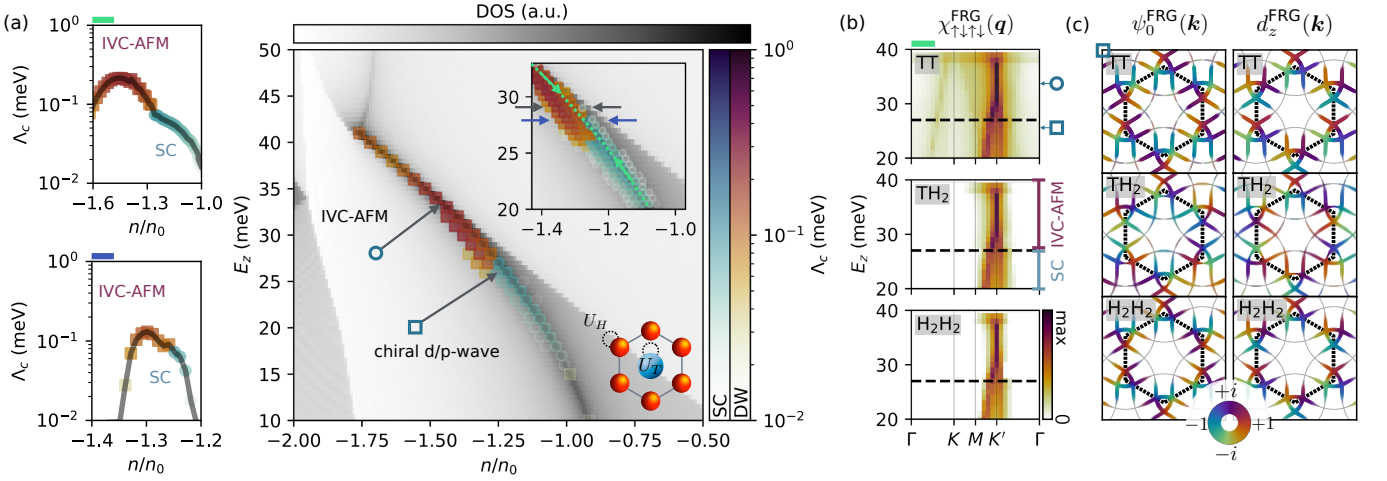


FIG. 2. FRG phase diagram of $\theta = 5.08^\circ$ tWSe₂ resolving the interplay of IVC-AFM order and chiral d/p -wave superconductivity along the gate-tunable van-Hove singularity. (a) Main panel: FRG phase diagram as function of holes per moiré unit cell n/n_0 and external displacement field E_z . The phase diagram shows the critical scale Λ_c of the leading Fermi surface instability and indicates regimes of spin/charge density wave order (DW, red) and superconductivity (SC, blue). The density of states (DOS) is shown in the background (gray) to pinpoint the position of the van-Hove line. Close to the HOVHS (blue circle), the system features IVC-AFM order, while for lower values of the displacement field chiral d/p -wave superconductivity emerges on the van-Hove line. Inset: Zoom-in on the density-displacement field region where IVC-AFM order gives way to superconductivity. The colored arrows indicate different directions when moving along the van-Hove line (green arrows) or at constant displacement field cuts (grey, blue arrows). The critical scale Λ_c along these line cuts is shown in the panels on the left, indicating a maximal critical temperature of $\Lambda_c \sim 500$ mK that is reached in the immediate vicinity of the IVC-AFM phase. (b) Momentum structure and (in)commensurability of the IVC-AFM state along the van-Hove line. The subpanels show the absolute value of the particle-hole susceptibility $\chi_{\uparrow\downarrow\uparrow\downarrow}^{\text{FRG}}(\mathbf{q})$ at scale Λ_c for the relevant orbital components involving the Wannier orbitals T/H_2 . The leading momentum transfer \mathbf{Q}_C locks to K' at the HOVHS (blue circle) and successively shifts towards incommensurate momenta along the high symmetry path $K'-M$ when lowering the external displacement field along the van-Hove line (blue square). (c) Amplitude and phase dependence of the pairing instability at $E_z = 25$ meV (blue circle) decomposed into singlet $\psi_0(\mathbf{k})$ and triplet $d_z(\mathbf{k})$ components. The continuous colorbar indicates the relative phase, whereas the amplitude is encoded by the opacity. The SC order parameter is two-fold degenerate and likely minimizes its free energy by the chiral superposition $d + id/p + ip$.

or a particle-hole instability as well as the momentum, spin/valley and orbital structure of the order parameter. Since we choose the sharp frequency cutoff as regulator (as implemented in the divERGE library [88]), the critical scale Λ_c serves as a proxy for the critical temperature of the transition (further details on FRG are given in the SM [75]).

III. FRG PHASE DIAGRAM

We present the FRG phase diagram of 5.08° tWSe₂ in Fig. 2 (a), where we plot the critical scale Λ_c of emergent particle-particle (blue) and particle-hole (red) instabilities as a function of hole filling per moiré unit cell n/n_0 and transverse electrical field E_z . The density of states (DOS) is shown as a reference to pinpoint the position of the van-Hove line (gray). At the position of the HOVHS, the system promotes an inter-valley coherent (IVC) anti-ferromagnetic spin-density wave with order parameter

$$\vec{\Delta}_{\mathbf{R}}^{\text{AFM}} \propto \sum_{X \in \{T, H_2\}} e^{i[\mathbf{Q}_C \cdot \mathbf{R} + i\vartheta_X]} \langle c_{\mathbf{R}X}^{\nu\dagger} \vec{\sigma}^{\nu\nu'} c_{\mathbf{R}X}^{\nu} \rangle + \text{h.c.}, \quad (2)$$

where $\vec{\sigma}$ acts in the space of the locked spin-valley degree of freedom and ϑ_X measures the relative orientation and weight of the 120° in-plane spin orientation on the orbitals T/H_2 that is otherwise arbitrary due to the remaining $U_\nu(1)$ symmetry. The spin density wave breaks translational invariance due to the finite transfer momentum $\mathbf{Q}_C = K^\nu$ that connects the HOVHSs in different spin-valley sectors and transforms in the trivial A irreducible representation (IR) of the C_{3z} little group at K^ν . Consistent with the orbital polarization of the Fermi pockets at the HOVHS, the order parameter has dominant weight on the T/H_2 -orbitals as imprinted in the transverse particle-hole susceptibility $\chi_{\uparrow\downarrow\uparrow\downarrow}^{\text{FRG}}(\mathbf{q})$ (see SM [75] for details) shown in Fig. 2 (b). Decreasing the value of the displacement field along the van-Hove line shifts the leading momentum transfer \mathbf{Q}_C towards the M -point, causing regions of incommensurate IVC-AFM order as demonstrated in Fig. 2 (b).

The absence of a perfect scattering vector that connects the van-Hove points in different spin-valley sectors and the reduction of the DOS weakens particle-hole instabilities for $E_z < E_z^c$ and instead promotes the effect of particle-particle fluctuations leading to the for-

mation of superconductivity along the van-Hove line, see blue square in Fig. 2 (a). The formation of superconductivity along the van-Hove line is hence facilitated by Fermi surface warping when detuning the system from the HOVHS, reminiscent of pairing in the t - t' square lattice Hubbard model [89] as will be discussed in Section IV A in more detail.

The Ising-like spin-orbit coupling in t WSe₂ couples singlet- and triplet components of the superconducting order parameter

$$\hat{\Delta}^{\text{SC}}(\mathbf{k}) = \left[\hat{\psi}_0(\mathbf{k})\sigma_0 + \vec{d}(\mathbf{k}) \cdot \vec{\sigma} \right] i\sigma_y, \quad (3)$$

where the hat-symbol encodes the orbital and spin-valley degree of freedom. We find that the leading superconducting order parameter is an inter-valley symmetric combination ($S^z = 0$) of singlet and triplet components $[\psi_0(\mathbf{k}), d_z(\mathbf{k})]$ that are allowed to admix due to the preserved $U_\nu(1)$ symmetry [39]. The Fermi surface projected amplitude and phase of the respective components is shown in the right panel of Fig. 2 (c). The leading order parameter transforms in the two-dimensional E irreducible representation of the Hamiltonian's point group \mathcal{G}_0 . In a mean-field picture, the two degenerate order parameters are in general superimposed and the free energy is presumably minimized by the chiral, time-reversal breaking combination $d \pm id/p \pm ip$. The latter gaps the Fermi surface and hence minimizes the energy of the superconducting condensate [89–93]. The chiral superconducting state belongs to the A Cartan (Altland-Zirnbauer) class for S_z preserving Bogoliubov de-Gennes Hamiltonians [94] possessing a \mathbb{Z} topological invariant that manifests in a non-vanishing Chern number $C = \pm 2$ and edge modes that are described by Dirac-like complex fermionic quasiparticle.

Besides the microscopic characterization of the emergent phases, a central question of recent experimental measurements concerns their interplay along the displacement field tunable van-Hove line that is captured by the unbiased FRG analysis. To this end, the inset of Fig. 2 (a) details the transition region of the phase diagram from the intervalley-coherent (IVC) antiferromagnet (AFM) to the chiral d/p -wave superconductor. We further provide line cuts of the phase diagram along the van-Hove line (green dash) and for cuts with constant displacement field (blue/gray dash) in Fig. 2 (a). We find that the highest transition temperature of the superconducting state $\Lambda_c \sim 500$ mK is reached in the immediate vicinity to the (incommensurate) IVC-AFM phase along the van-Hove line. The superconducting region flanks the IVC-AFM state and we observe an asymmetry of spin-ordered regimes with respect to the van-Hove line, i.e. instabilities occur at larger critical scales Λ_c for $n < n_{\text{VHS}}$ and $E_z < E_z^c$ in agreement with experimental observations [37, 38]. The following two Sections are devoted to (i) unraveling the role of IVC-AFM spin-fluctuations in the formation of chiral d/p -wave superconductivity and to (ii) tying the observed asymmetry of particle-hole in-

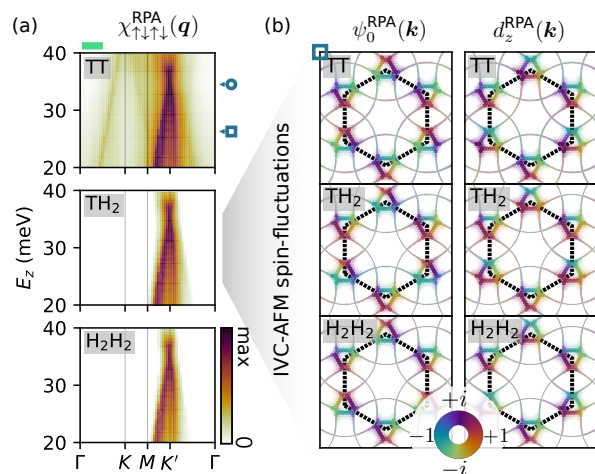


FIG. 3. IVC-AFM spin fluctuation mechanism to unconventional superconductivity in t WSe₂ by commensurate to incommensurate transition. (a) Absolute value of the RPA-renormalized susceptibility $\chi_{\uparrow\downarrow\uparrow\downarrow}^{\text{RPA}}(\mathbf{q})$ at the critical interaction strength $\alpha_c U$ involving the dominant Wannier orbitals T/H_2 . The leading momentum transfer \mathbf{Q}_C locks to K' at the HOVHS (blue circle) and successively shifts towards incommensurate momenta along the high symmetry path $K'-M$ when lowering the external displacement field along the van-Hove line (blue square). (b) Fluctuations around the (incommensurate) IVC-AFM order give rise to chiral d/p -wave superconductivity comprising an equal mixture of spin-singlet $\psi_0^{\text{RPA}}(\mathbf{k})$ and spin-triplet $d_z^{\text{RPA}}(\mathbf{k})$ weight in the order parameter. For $E_z \sim 25$ meV (blue square), the phase of the resulting order parameter is indicated by the circular colorbar and the amplitude (projected on the Fermi surface) is encoded by the opacity. The superconducting order parameter only has notable weight on the triangular pockets around K^ν , whereas the superconducting amplitude vanishes on the larger Fermi arcs connecting neighboring K^ν points.

stabilities to the fermiology of the flat bands of t WSe₂.

IV. MECHANISM TO SUPERCONDUCTIVITY

A. Spin-fluctuation exchange as pairing mechanism in t WSe₂

To unravel the microscopic mechanism that supports superconductivity along the van-Hove line, we switch off inter-channel coupling of the full FRG flow equations and thereby arrive at a single-channel RPA resummation of the interaction in the crossed particle-hole channel

$$C_U^{\text{RPA}}(\mathbf{q}) = \hat{U} \hat{\chi}^{\text{RPA}}(\mathbf{q}) \hat{U} = \hat{U} [\mathbb{1} - \hat{U} \hat{\chi}^0(\mathbf{q})]^{-1}. \quad (4)$$

This procedure segregates spin fluctuations from other possible fluctuations captured by the FRG. The resulting RPA-renormalized particle-hole susceptibility $\hat{\chi}_{\uparrow\downarrow\uparrow\downarrow}^{\text{RPA}}(\mathbf{q})$ at scale $\Lambda = 0.1$ meV is shown in Fig. 3 (a). As expected from the Fermi surface sheets in the different spin-valley sectors, c.f. Fig. 1 (c), the dominant ordering vector \mathbf{Q}_C

locks to K^ν at the HOVHS (blue circle) and successively shifts towards incommensurate momenta on the K^ν - M line when lowering the external displacement field E_z . In this regime, the Fermi surface consists of triangular pockets around K^ν featuring three inequivalent van-Hove points associated to the three neighboring M -points, see Fig. 1 (c). Scattering between the van-Hove points enhances the particle-hole susceptibility leading to a pronounced commensurate-to-incommensurate transition of the IVC-AFM state along the van-Hove line, which is in good agreement with the interacting particle-hole susceptibility obtained from the full-fledged FRG treatment shown in Fig. 2 (b). To address pairing instabilities originating from fluctuations around the (incommensurate) IVC-AFM order that are present in the paramagnetic normal-state, we construct an effective pairing vertex $\Gamma^P(\mathbf{k}_P, \mathbf{k}'_P)$ from the RPA renormalized interaction in the exchange channel [95, 96] and analyze the symmetry of the leading superconducting order parameter by solving a linearized gap equation in orbital space, see SM [75] for technical details. As shown in Fig. 3 (b), we find a superconducting state with mixed-parity that transforms in the two-dimensional E irreducible representation (d/p -wave) in leading order for all values of the displacement field, exemplified for $E_z = 25$ meV (blue square). The superconducting order parameter is enhanced on the triangular Fermi pockets around K^ν that are exclusively T/H_2 polarized. Meanwhile, the amplitude of the SC order parameter is significantly suppressed if pairing involves Bloch states associated to the Wannier orbital H_1 . This manifests in a vanishing SC amplitude on the larger Fermi surface arcs that connect neighboring K^ν points, c.f. Fig. 1 (c). Therefore, we expect that the superconducting state is effectively gapless over large parts of the Fermi surface leading to nodal signatures in spectroscopy measurements. The emergence of superconductivity from spin-fluctuation exchange can be understood by the real-space structure of the effective RPA pairing vertex $\Gamma^P(\mathbf{k}_P, \mathbf{k}'_P)$ that features attractive components on bonds connecting neighboring (T, H_2) orbitals such to overcome the initially repulsive Coulomb interaction. As the phenomenology of the IVC-AFM state and the symmetry of the superconducting order parameter accurately agrees with the FRG results, we argue that spin fluctuations represent the pairing glue for electron-mediated superconductivity observed in tWSe₂ along the van-Hove line.

B. Asymmetry of particle-hole instabilities by Fermi surface broadening induced nesting

An interesting observation of recent experiments [37, 38] concerns the apparent asymmetry of instabilities with respect to the displacement field tunable VHS that also manifests in the FRG phase diagram, i.e. (i) the maximal transition temperature of the IVC-AFM phase is encountered for values of the displacement field below

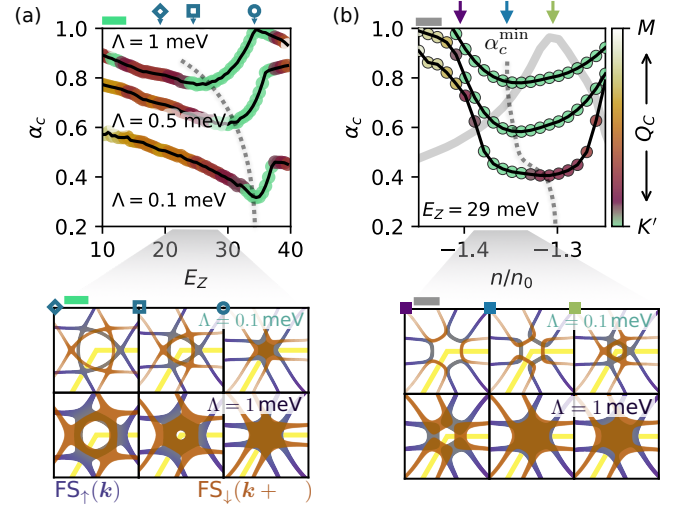


FIG. 4. Asymmetry of particle-hole instabilities due to Fermi surface broadening induced nesting. (a) Critical (relative) interaction scale α_c of the RPA renormalized interaction for different scales Λ along the van-Hove line. The leading momentum transfer Q_C along the high symmetry path K^ν - M is encoded by the colorbar shared among panels (a,b). The minimal value of α_c for each curve is indicated by the grey dashed line showing a clear asymmetry of particle-hole instabilities with respect to the position of the HOVHS (blue circle). The lower panel shows the (Λ -broadened) Fermi surface sheets of the spin-valley polarized sub-sectors, i.e., all eigenenergies that are within the energy shell $[E_F - \Lambda, E_F + \Lambda]$ around the Fermi energy E_F . (b) Same information as in panel (a), taken for the constant displacement field cut $E_z = 29$ meV as indicated by the grey arrows in Fig. 2 (a). The grey solid line indicates the DOS as the density n/n_0 is varied across the van-Hove line. For low scales, the minimal value of α_c (grey dashed line) is encountered on the van-Hove line (green arrow) and the leading momentum transfer Q_c is displaced from K^ν . At larger scales, α_c^{\min} is shifted to larger hole fillings and Q_c locks back to K^ν .

the position of the HOVHS and (ii) instabilities are enhanced for $n < n_{VHS}$, but diminish for $n > n_{VHS}$. Here, we demonstrate that in the weak-to-moderate interacting regime, this asymmetry is related to scale-dependent nesting properties of the Fermi surface [97, 98] that lead to commensurability locking of particle-hole instabilities away from the van-Hove line. To analyze the aforementioned asymmetric behavior, we again concentrate on a single-channel RPA resummation in the crossed particle-hole channel and calculate the critical (relative) interaction strength α_c defined by the divergence of the RPA renormalized interaction $C_U^{\text{RPA}}(\mathbf{q})$ [cf. Eq. (4)], i.e., $\det[\mathbb{1} - \alpha_c \hat{U} \hat{\chi}^0(\mathbf{q})] = 0$. Figure 4 (a) displays the critical value α_c and the leading momentum transfer Q_C of the (incommensurate) IVC-AFM state along the van-Hove line for different RG scales Λ . The latter enters the RPA theory as temperature in the Fermi-Dirac statistics and hence determines the smearing of states in the vicinity of the Fermi energy, see SM [75] for technical details. At

low scale $\Lambda = 0.1$ meV, the minimal critical interaction α_c^{\min} (gray dashed line) is found at the HOVHS (blue circle), where the leading momentum transfer of the associated IVC-AFM state locks to $\mathbf{Q}_C = K^\nu$. This finding is consistent with the enhanced DOS at the HOVHS and the fact that the vector $\mathbf{q} = K^\nu$ perfectly connects Fermi surface sheets (FS) of opposite spin-valley polarization. To this end, we show the Λ -broadened FS, i.e., all eigenenergies that reside within the energy shell $[E_F - \Lambda, E_F + \Lambda]$ around the Fermi energy E_F , in the lower panel of Fig. 4 (a). Lowering the displacement field continuously displaces \mathbf{Q}_C towards the M -point and increases the critical interaction strength α_c as scattering between the triangular FS pockets around K^ν is suppressed due to the relative orientation mismatch of the van-Hove points in different spin-valley sectors. At larger scales $\Lambda = \{0.5, 1.0\}$ meV, however, the suppression of particle-hole instabilities for $E_z < E_z^c$ and the associated shift of \mathbf{Q}_C towards the M -point are counteracted by the induced smearing of the triangular FS pockets formed by the three van-Hove points. Lowering the displacement field along the van-Hove line (left panel) increases the size of the FS pockets around K^ν such that scattering with vector $\mathbf{Q}_C = K^\nu$ between FS sheets of opposite spin-valley polarization is (re)enhanced at larger scales Λ . As a consequence of the higher scale Λ , the minimal critical value α_c^{\min} moves to lower values of the displacement field along the van-Hove line. This causes an asymmetry of interaction-induced particle-hole instabilities with respect to the HOVHS.

A similar asymmetry is encountered when varying the hole density n/n_0 for constant values of the displacement field $E_z < E_z^c$ as demonstrated in Fig. 4 (b). To show this, we focus on $E_z = 29$ meV (gray dash), where the asymmetry is maximal in the FRG phase diagram as demonstrated in Fig. 2 (a). In this regime, the Fermi surface at the VHS ($n_{\text{VHS}} \sim -1.3$, green arrow) consists of three van-Hove points that are displaced from K^ν such that the leading momentum transfer \mathbf{Q}_C is shifted towards the M -point. Decreasing the hole density lifts the van-Hove points and increases the size of the (open) FS pockets, similar to the observed phenomenology when varying the displacement field along the van-Hove line. For larger scales (temperatures), the broadening of the FS pockets (re)enhances scattering processes with momentum transfer $\mathbf{Q}_C = K^\nu$ and the minimal critical interaction strength α_c^{\min} is moved to hole densities $n < n_{\text{VHS}}$.

In conclusion, we argue that the minimal critical interaction α_c^{\min} is shifted to lower displacement fields $E_z < E_z^c$ and lower densities $n < n_{\text{VHS}}$ with respect to the position of the HOVHS and the displacement field tunable van-Hove line when particle-hole instabilities are encountered at non-zero temperature, or higher scales Λ . As the critical scale Λ_c of particle-hole instabilities encountered in the FRG flow depends primarily on the strength of the Hubbard interactions U_X in Eq. (1), it is an indicator for how strongly coupled the system under

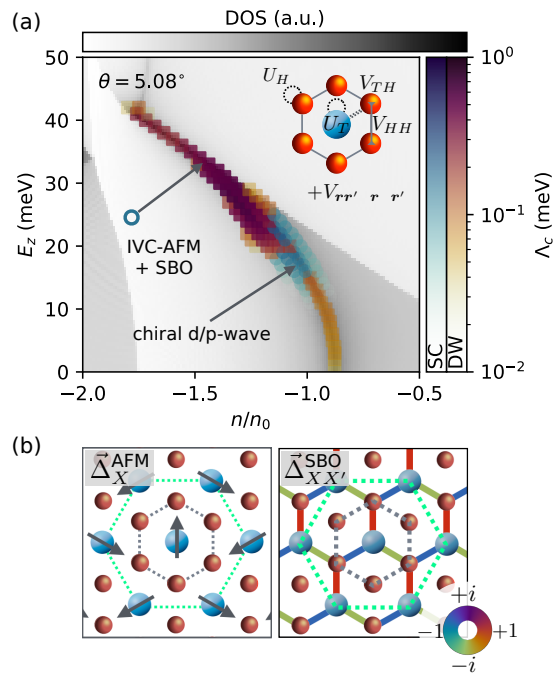


FIG. 5. Influence of long-ranged density-density interactions on the low-energy phase diagram of $\theta = 5.08^\circ$ tWSe₂. (a) FRG phase diagram as function of holes per moiré unit cell n/n_0 and external displacement field E_z . The on-site IVC-AFM order parameter mixes with a spin-bond order (SBO) parameter between the T/H_2 orbitals that transform in the A -IR of C_{3z} . This raises the critical scale Λ_c of the density wave (DW) instabilities in the phase diagram and enhances the critical temperature of the superconducting phase. (b) Real-space structure of the particle-hole instabilities. The (magnetic) Wigner-Seitz cell is indicated by the (green) gray dashed line.

scrutiny is. Therefore, it is expected that the observed asymmetry is enhanced when increasing the strength of the interactions relative to the bandwidth. This can be achieved by tuning the twist angle (see Section VI) or altering the dielectric environment, i.e., changing the distance to metallic gates. We further note that the scale-dependent nesting properties of tWSe₂ are tied to microscopic details of the fermiology of the system, particularly the formation of the triangular FS pockets around K^ν and the flat regions in momentum space originating from the HOVHS. This asymmetric occurrence of particle-hole instabilities and the associated commensurability locking may hence not be unique to tWSe₂, but appear generically in systems with tunable FS pockets and HOVHS.

V. INFLUENCE OF LONG-RANGED INTERACTIONS: FORMATION OF SPIN-BOND ORDER

Besides the dominant Hubbard interaction terms acting on the triangular (T) and honeycomb sites ($H_{1,2}$)

of the effective Wannier model defined in Eq. (1), the ratio between the Wannier function spread $\Omega \sim |\mathbf{a}_M| = 3.74 \text{ nm}$ and the distance to the metallic gates $\xi \sim 10 \text{ nm}$ on either side of the sample suggests that longer-ranged density-density interactions impact the low-energy physics of $\theta = 5.08^\circ$ tWSe₂. Meanwhile, exchange and pair-hopping contributions between neighboring Wannier orbitals are negligible as expected from the exponential localization of the Wannier orbitals, see SM [75]. Therefore, we next complement the Hubbard Hamiltonian Eq. (1) by density-density terms that are obtained when projecting the dual-gated Coulomb interaction to the Wannier basis:

$$H^V = H + \sum_{\nu, \mu} \sum_{X, X' \in \{T, H_1, H_2\}} \sum_{\mathbf{R}, \mathbf{R}'} V_{XX'}^{\mathbf{R}\mathbf{R}'} n_{\mathbf{R}X}^\nu n_{\mathbf{R}'X'}^\mu. \quad (5)$$

In the spirit of an *ab-initio* characterization of correlated phases in tWSe₂, we consider the full real-space dependence of $V_{XX'}^{\mathbf{R}\mathbf{R}'}$ in this Section. The largest of these density-density terms are the nearest-neighbor honeycomb-triangular (honeycomb-honeycomb) density-density interactions $V_{TH} \approx 33 \text{ meV}$ ($V_{HH} \approx 28 \text{ meV}$). We demonstrate in the SM [75] that truncating Eq. 5 after these terms already qualitatively accounts for the effects of longer-range interactions observed below.

The corresponding FRG phase diagram for $\theta = 5.08^\circ$ tWSe₂ is shown in Fig. 5 (a). While the qualitative features of the phase diagram resemble those of the pristine Hubbard model Eq. (1), the phase boundaries and critical scales of the emergent particle-hole (particle-particle) instabilities are altered. The observed quantitative changes arise because the inter-site interaction causes non-local particle-hole pairs to get admixed to the local IVC-AFM order parameter. The nearest-neighbor repulsion between triangular (T) and honeycomb (H_2) orbitals supports the formation of a spin/valley-bond order (SBO)

$$\vec{\Delta}_{\mathbf{R}, \mathbf{R}'}^{\text{SBO}} \propto e^{i\mathbf{Q}_C \cdot \mathbf{R}} \langle c_{\mathbf{R}, T}^{\nu\dagger} \bar{\sigma}^{\nu\nu'} c_{\mathbf{R}', H_2}^{\nu'} \rangle + \text{h.c.} \quad (6)$$

The SBO transforms within the trivial A -irreducible representation (IR) of the little group C_{3z} at K^ν and is therefore symmetry-allowed to mix with the IVC-AFM state Δ^{AFM} driven by the on-site Hubbard repulsion. In Fig. 5 (b), we present a sketch of the magnetization patterns in the IVC-AFM+SBO phase comprising an on-site 120° spin configuration as well as the bond order component between T - H_2 . Note that due to the p_ν -orbital character of the H_2 -orbital, the bonds feature a relative phase of $\omega = e^{2\pi i/3}$ between C_{3z} -related H_2 -orbitals. The gain in free energy arises because the projection of the bare nearest-neighbor repulsion $V_{TH(HH)}$ to the crossed particle-hole channel lowers the energy of states with an SBO component of the order:

$$\Delta^{\text{SBO}*} \circ C[\Gamma_{\Lambda=\infty}^{(4)}] \circ \Delta^{\text{SBO}} > 0, \quad (7)$$

see SM [75] for details. The non-vanishing SBO components in the order parameter hence promote the formation of particle-hole pairs at larger critical scales Λ_c as

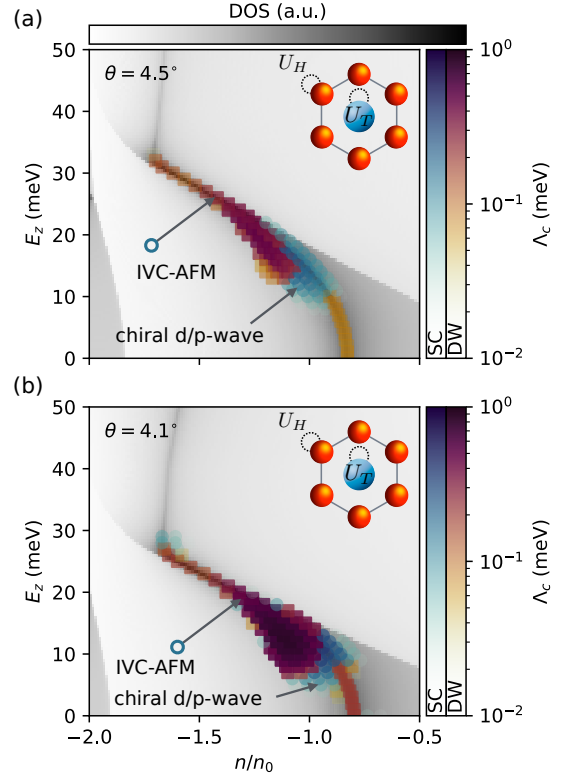


FIG. 6. Evolution of IVC-AFM domains and SC order in the low-energy phase diagram of tWSe₂ in the intermediate twist angle regime $\theta = 4^\circ \dots 5^\circ$. (a) FRG phase diagram at $\theta = 4.5^\circ$ tWSe₂ considering Hubbard-type interactions on the triangular (T) and honeycomb ($H_{1,2}$) orbitals. The blue circle indicates the position of the HOVHS. Regions of IVC-AFM order evolve to smaller absolute values of the displacement field E_z and larger critical scales signaling the onset of correlated states at higher critical temperatures $\Lambda_c \sim T_c$. The maximal critical scale Λ_c^{max} features a pronounced asymmetry with respect to the HOVHS (blue circle) and the tunable van-Hove line (grey). (b) FRG phase diagram at $\theta = 4.1^\circ$. Reaching the moderate-to-strongly interacting regime, the critical scales of IVC-AFM and chiral d/p -wave superconductivity are further enhanced. As a consequence, regions of SC order in the $E_z - n/n_0$ phase diagram are shrunk in size in favor of IVC-AFM ordered regions that move towards $n/n_0 \sim 1$.

demonstrated in Fig. 5 (a) [compare with Fig. 2 (a)]. We therefore argue that the particle-hole instability experiences an effective anti-screening by virtue of long-ranged density-density type interactions. The coupling to the on-site IVC-AFM order that drives the chiral p/d -wave pairing instability causes the maximal critical temperature to rise to $\Lambda_c \sim 1 \text{ K}$. Meanwhile, the size of the SC region in the phase diagram is decreased due to the competition with the IVC-AFM state.

VI. EVOLUTION OF THE SC PHASE IN THE INTERMEDIATE TWIST ANGLE REGIME

Finally, we map out phase diagrams in the intermediate twist angle regime $\theta = \{4.1^\circ, 4.5^\circ\}$ as summarized in Fig. 6 (a,b). Decreasing the twist angle quenches the kinetic energy scales such that the moiré bands react more sensitively to the external displacement field. As a result, the position of the HOVHS is moved to smaller values of E_z , see blue circle in Fig. 5 (c,d) and SM [75]. As the ratio between the Wannier function spread and the gate screening distance Ω/ξ decreases with the twist angle, long-ranged density-density interaction between the Wannier orbitals are successively suppressed and we therefore resort to the Hubbard Hamiltonian defined in Eq. (1). The values of the Hubbard interactions for different twist angles are listed in the SM [75].

Apart from the enhanced impact of the displacement field on the single-particle bandstructure, decreasing the twist angle increases the ratio U/W and places the system in a moderate interacting regime. As a consequence, the emergent IVC-AFM state and the chiral d/p -wave SC state manifest at larger scales Λ_c indicating a higher critical temperature of respective phases. Consistent with the analysis brought forward in Section IV B, this enhances the asymmetry of the IVC-AFM with respect to the van-Hove line as demonstrated in Fig. 6 (a,b). At $\theta = 4.5^\circ$, the maximal critical scale Λ_c of the IVC-AFM phase is found around $E_z \sim 15$ meV and is clearly displaced from the van-Hove line, where instead regions of chiral d/p -wave SC prevail. At $\theta = 4.1^\circ$ the IVC-AFM state is displaced to the vicinity of $n/n_0 \sim 1$ and the superconducting region is shrunk in size; a trend that is observed in small twist angle tWSe₂ in Ref. [37]. In particular, superconductivity does not extend to $E_z = 0$ meV, but is tied to an intermediate displacement field regime $5 \text{ meV} < E_z < 10 \text{ meV}$.

VII. CONCLUSION AND OUTLOOK

In this work, we provide a complete and unbiased characterization of correlated states in $\theta = 4^\circ \dots 5^\circ$ tWSe₂ from *first principles* by studying the impact of gate-screened Coulomb interactions with state-of-the-art functional renormalization group techniques. Our analysis reveals that inter-valley coherent anti-ferromagnetic order (IVC-AFM) and chiral, mixed-parity d/p -wave superconductivity collaborate along the gate-tunable van-Hove line. The superconducting pairing glue for the unconventional SC state is provided by spin-fluctuations arising in regions of incommensurate IVC-AFM order below the HOVHS, where the Fermi surface pockets around the valleys K^ν are broadened and therefore weaken scattering between opposite spin-valley sectors. We attribute the asymmetry of particle-hole instabilities observed in experiment [37, 38] to the formation of hole pockets around K^ν that are broadened at larger scales (tem-

perature) such that the dominant ordering vector locks back to K^ν at positions that are offset from the van-Hove line [99]. As the hole pockets are equally polarized on the T/H_2 -orbital, this stresses the importance of describing the low-energy physics of tWSe₂ in the multi-orbital setup presented in this manuscript. One aspect of the experiment of Guo *et. al.* [38] that is however not clearly reproduced by our calculations is the non-monotonic variation of antiferromagnetism with carrier concentration at fixed displacement field. At displacement fields slightly greater than those where superconductivity is observed, experiment finds evidence for antiferromagnetism at carrier concentrations slightly lower than and slightly higher than the van-Hove concentrations, but not when the carrier density is tuned to the van-Hove concentration. Understanding this behavior is an important topic for future research. Further, we demonstrate that long-ranged density-density interactions do not alter the phase diagram of tWSe₂ qualitatively, but change the phase boundaries and critical temperature due to the coupling of the IVC-AFM order parameter to a spin/valley bond order (SBO) that acts as an interaction-induced spin-orbit coupling term. We therefore argue that the presence of longer-ranged density-density interactions will enhance the critical temperature T_c of the SC phase, however, decrease its overall size in the phase diagram due to the competition with the IVC-AFM state.

Finally, we show that as the twist angle is decreased to $\theta = 4.1^\circ$ the regions of SC order are displaced to smaller values of the external displacement field ($5 \text{ meV} < E_z < 10 \text{ meV}$) and to hole densities closer to $n/n_0 \sim 1$ in good agreement with experimental measurements. It is interesting to consider these results in light of the finding of Xia *et. al.* [37] that in a $\theta = 3.65^\circ$ angle device, a superconducting region exists very near $n/n_0 = 1$ and vanishing displacement field, giving way to an insulating phase as the displacement field is increased. Whether this superconductor-insulator transition is a consequence of strong coupling Mott/spin liquid physics or can be understood within the weak-to-moderate coupling physics captured by the FRG approach used here is an important open question.

The validity of the static four-point FRG employed in this work is bound to the weak to moderate interacting regime $U/W < 1$ that is relevant for the twist angles considered within this work. By further decreasing the twist angle, we expect that the system is eventually tuned into a strongly interacting regime. It is thus a highly anticipated avenue of future research to treat this regime with state-of-the-art methods such as, e.g. DMFT or slave Bosons to learn about the properties of strongly correlated and ordered states in tWSe₂.

ACKNOWLEDGMENTS

This work was supported by the Excellence Initiative of the German federal and state governments, the Ministry of Innovation of North Rhine-Westphalia and the Deutsche Forschungsgemeinschaft (DFG, German Research Foundation). AF and DMK acknowledge funding by the DFG within the Priority Program SPP 2244 “2DMP” – 443274199. LK acknowledges support from the DFG through Project-ID 258499086 – SFB 1170 and through the Würzburg-Dresden Cluster of Excellence on Complexity and Topology in Quantum Matter – ct.qmat, Project-ID 390858490 – EXC 2147. LK and TOW gratefully acknowledge support from the DFG through FOR 5249 (QUAST, Project No. 449872909) and SPP 2244 (Project No. 422707584). SR is supported by the DFG research unit FOR 5242 (WE 5342/7-1, project No. 449119662). TOW is supported by the Cluster of Excellence “CUI: Advanced Imaging of Matter” of the DFG (EXC 2056, Project ID 390715994). AR acknowledges support by the European Research Council (ERC-2015-

AdG694097), the Cluster of Excellence ‘Advanced Imaging of Matter’ (AIM), Grupos Consolidados (IT1249-19) and Deutsche Forschungsgemeinschaft (DFG) – SFB-925 – project 170620586. LX acknowledges supported by the National Key Research and Development Program of China (Grant No. 2022YFA1403501), Guangdong Basic and Applied Basic Research Foundation (Grant No. 2022B1515120020), the National Natural Science Foundation of China (Grant No. 62341404), Hangzhou Tsientang Education Foundation and the Max Planck Partner group programme. AJM acknowledges support from Programmable Quantum Materials, an Energy Frontier Research Center funded by the U.S. Department of Energy (DOE), Office of Science, Basic Energy Sciences (BES), under award (DE-SC0019443). DMK and AR acknowledge support by the Max Planck-New York City Center for Nonequilibrium Quantum Phenomena. Computations were performed on the HPC system Ada at the Max Planck Computing and Data Facility. The Flatiron Institute is a division of the Simons Foundation.

-
- [1] D. M. Kennes, M. Claassen, L. Xian, A. Georges, A. J. Millis, J. Hone, C. R. Dean, D. N. Basov, A. N. Pasupathy, and A. Rubio, *Nature Physics* **17**, 155–163 (2021).
- [2] L. Wang, E.-M. Shih, A. Ghiotto, L. Xian, D. A. Rhodes, C. Tan, M. Claassen, D. M. Kennes, Y. Bai, B. Kim, *et al.*, *Nature materials* **19**, 861 (2020).
- [3] Y. Xu, S. Liu, D. A. Rhodes, K. Watanabe, T. Taniguchi, J. Hone, V. Elser, K. F. Mak, and J. Shan, *Nature* **587**, 214 (2020).
- [4] X. Huang, T. Wang, S. Miao, C. Wang, Z. Li, Z. Lian, T. Taniguchi, K. Watanabe, S. Okamoto, D. Xiao, *et al.*, *Nature Physics* **17**, 715 (2021).
- [5] A. Ghiotto, L. Wei, L. Song, J. Zang, A. B. Tazi, D. Ostrom, K. Watanabe, T. Taniguchi, J. C. Hone, D. A. Rhodes, *et al.*, arXiv preprint arXiv:2405.17316 (2024).
- [6] E. Anderson, F.-R. Fan, J. Cai, W. Holtzmann, T. Taniguchi, K. Watanabe, D. Xiao, W. Yao, and X. Xu, *Science* **381**, 325 (2023).
- [7] V. Crépel and L. Fu, *Physical Review B* **107**, L201109 (2023).
- [8] Y. Zhang, T. Liu, and L. Fu, *Physical Review B* **103**, 155142 (2021).
- [9] S. Ryee and T. O. Wehling, *Nano Letters* **23**, 573 (2023), <https://doi.org/10.1021/acs.nanolett.2c04169>.
- [10] K. Slagle and L. Fu, *Physical Review B* **102**, 235423 (2020).
- [11] V. Crépel and L. Fu, *Science Advances* **7**, eabh2233 (2021).
- [12] I. Schwartz, Y. Shimazaki, C. Kuhlenkamp, K. Watanabe, T. Taniguchi, M. Kroner, and A. Imamoğlu, *Science* **374**, 336 (2021).
- [13] C. Kuhlenkamp, M. Knap, M. Wagner, R. Schmidt, and A. Imamoğlu, *Physical Review Letters* **129**, 037401 (2022).
- [14] V. Crépel, D. Guerci, J. Cano, J. Pixley, and A. Millis, *Physical review letters* **131**, 056001 (2023).
- [15] M. Wagner, R. Oldziejewski, F. Rose, V. Köder, C. Kuhlenkamp, A. Imamoğlu, and R. Schmidt, arXiv preprint arXiv:2310.08729 (2023).
- [16] H. Lange, L. Homeier, E. Demler, U. Schollwöck, A. Bohrdt, and F. Grusdt, *Physical Review B* **110**, L081113 (2024).
- [17] A. Ghiotto, E.-M. Shih, G. S. Pereira, D. A. Rhodes, B. Kim, J. Zang, A. J. Millis, K. Watanabe, T. Taniguchi, J. C. Hone, *et al.*, *Nature* **597**, 345 (2021).
- [18] T. Li, S. Jiang, L. Li, Y. Zhang, K. Kang, J. Zhu, K. Watanabe, T. Taniguchi, D. Chowdhury, L. Fu, *et al.*, *Nature* **597**, 350 (2021).
- [19] K. Tran, G. Moody, F. Wu, X. Lu, J. Choi, K. Kim, A. Rai, D. A. Sanchez, J. Quan, A. Singh, *et al.*, *Nature* **567**, 71 (2019).
- [20] L. Ma, P. X. Nguyen, Z. Wang, Y. Zeng, K. Watanabe, T. Taniguchi, A. H. MacDonald, K. F. Mak, and J. Shan, *Nature* **598**, 585 (2021).
- [21] J. Gu, L. Ma, S. Liu, K. Watanabe, T. Taniguchi, J. C. Hone, J. Shan, and K. F. Mak, *Nature physics* **18**, 395 (2022).
- [22] R. Xiong, J. H. Nie, S. L. Brantly, P. Hays, R. Sailus, K. Watanabe, T. Taniguchi, S. Tongay, and C. Jin, *Science* **380**, 860 (2023).
- [23] A. Dalal and J. Ruhman, *Physical Review Research* **3**, 043173 (2021).
- [24] D. Guerci, J. Wang, J. Zang, J. Cano, J. Pixley, and A. Millis, *Science Advances* **9**, eade7701 (2023).
- [25] W. Zhao, B. Shen, Z. Tao, Z. Han, K. Kang, K. Watanabe, T. Taniguchi, K. F. Mak, and J. Shan, *Nature* **616**, 61 (2023).
- [26] D. Guerci, K. P. Lucht, V. Crépel, J. Cano, J. Pixley, and A. Millis, *Physical Review B* **110**, 165128 (2024).
- [27] W. Zhao, B. Shen, Z. Tao, S. Kim, P. Knüppel, Z. Han, Y. Zhang, K. Watanabe, T. Taniguchi, D. Chowdhury, *et al.*, arXiv preprint arXiv:2310.06044 (2023).

- [28] F. Xie, L. Chen, and Q. Si, *Physical Review Research* **6**, 013219 (2024).
- [29] Z. Tao, B. Shen, S. Jiang, T. Li, L. Li, L. Ma, W. Zhao, J. Hu, K. Pistunova, K. Watanabe, *et al.*, *Physical Review X* **14**, 011004 (2024).
- [30] K. Kang, Y. Qiu, K. Watanabe, T. Taniguchi, J. Shan, and K. F. Mak, *Nano Letters* (2024).
- [31] Y. Zeng, Z. Xia, K. Kang, J. Zhu, P. Knüppel, C. Vaswani, K. Watanabe, T. Taniguchi, K. F. Mak, and J. Shan, *Nature* **622**, 69 (2023).
- [32] J. Cai, E. Anderson, C. Wang, X. Zhang, X. Liu, W. Holtzmann, Y. Zhang, F. Fan, T. Taniguchi, K. Watanabe, *et al.*, *Nature* **622**, 63 (2023).
- [33] F. Xu, Z. Sun, T. Jia, C. Liu, C. Xu, C. Li, Y. Gu, K. Watanabe, T. Taniguchi, B. Tong, *et al.*, *Physical Review X* **13**, 031037 (2023).
- [34] H. Park, J. Cai, E. Anderson, Y. Zhang, J. Zhu, X. Liu, C. Wang, W. Holtzmann, C. Hu, Z. Liu, *et al.*, *Nature* **622**, 74 (2023).
- [35] K. Kang, B. Shen, Y. Qiu, Y. Zeng, Z. Xia, K. Watanabe, T. Taniguchi, J. Shan, and K. F. Mak, *Nature* **628**, 522 (2024).
- [36] V. Crépel and A. Millis, *Physical Review Letters* **133**, 146503 (2024).
- [37] Y. Xia, Z. Han, K. Watanabe, T. Taniguchi, J. Shan, and K. F. Mak, arXiv preprint arXiv:2405.14784 (2024).
- [38] Y. Guo, J. Pack, J. Swann, L. Holtzman, M. Cothrine, K. Watanabe, T. Taniguchi, D. Mandrus, K. Barmak, J. Hone, *et al.*, arXiv preprint arXiv:2406.03418 (2024).
- [39] C. Schrade and L. Fu, arXiv preprint arXiv:2110.10172 (2021).
- [40] A. Wietek, J. Wang, J. Zang, J. Cano, A. Georges, and A. Millis, *Physical Review Research* **4**, 043048 (2022).
- [41] L. Klebl, A. Fischer, L. Classen, M. M. Scherer, and D. M. Kennes, *Physical Review Research* **5**, L012034 (2023).
- [42] S. Kim, J. F. Mendez-Valderrama, X. Wang, and D. Chowdhury, arXiv preprint arXiv:2406.03525 (2024).
- [43] J. Zhu, Y.-Z. Chou, M. Xie, and S. D. Sarma, arXiv preprint arXiv:2406.19348 (2024).
- [44] M. Christos, P. M. Bonetti, and M. S. Scheurer, arXiv preprint arXiv:2407.02393 (2024).
- [45] D. Guerci, D. Kaplan, J. Ingham, J. Pixley, and A. J. Millis, arXiv preprint arXiv:2408.16075 (2024).
- [46] C. Tuo, M.-R. Li, Z. Wu, W. Sun, and H. Yao, “Theory of topological superconductivity and antiferromagnetic correlated insulators in twisted bilayer wse_2 ,” (2024), arXiv:2409.06779 [cond-mat.str-el].
- [47] A. V. Chubukov and C. M. Varma, “Quantum-criticality and superconductivity in twisted transition metal di-chalcogenides,” (2024), arXiv:2410.10038 [cond-mat.supr-con].
- [48] F. Xie, L. Chen, S. Sur, Y. Fang, J. Cano, and Q. Si, “Superconductivity in twisted wse_2 from topology-induced quantum fluctuations,” (2024), arXiv:2408.10185 [cond-mat.str-el].
- [49] W. Qin, W.-X. Qiu, and F. Wu, “Kohn-luttinger mechanism of superconductivity in twisted bilayer wse_2 : Gate-tunable unconventional pairing symmetry,” (2024), arXiv:2409.16114 [cond-mat.supr-con].
- [50] R. S. Mong, D. J. Clarke, J. Alicea, N. H. Lindner, P. Fendley, C. Nayak, Y. Oreg, A. Stern, E. Berg, K. Shtengel, *et al.*, *Physical Review X* **4**, 011036 (2014).
- [51] A. Vaezi, *Physical Review X* **4**, 031009 (2014).
- [52] M. Barkeshli, *Physical review letters* **117**, 096803 (2016).
- [53] V. Crépel and N. Regnault, arXiv preprint arXiv:2403.05622 (2024).
- [54] F. Wu, T. Lovorn, E. Tutuc, I. Martin, and A. MacDonald, *Physical review letters* **122**, 086402 (2019).
- [55] T. Devakul, V. Crépel, Y. Zhang, and L. Fu, *Nature communications* **12**, 6730 (2021).
- [56] Z. Bi and L. Fu, *Nature communications* **12**, 642 (2021).
- [57] V. Crépel and A. Millis, *Physical Review Research* **6**, 033127 (2024).
- [58] X.-W. Zhang, C. Wang, X. Liu, Y. Fan, T. Cao, and D. Xiao, *Nature Communications* **15** (2024), 10.1038/s41467-024-48511-x.
- [59] W.-X. Qiu, B. Li, X.-J. Luo, and F. Wu, *Phys. Rev. X* **13**, 041026 (2023).
- [60] M. Salmhofer and C. Honerkamp, *Progress of Theoretical Physics* **105**, 1 (2001), <https://academic.oup.com/ptp/article-pdf/105/1/1/5164880/105-1-1.pdf>.
- [61] W. Metzner, M. Salmhofer, C. Honerkamp, V. Meden, and K. Schönhammer, *Rev. Mod. Phys.* **84**, 299 (2012).
- [62] C. Platt, W. Hanke, and R. Thomale, *Advances in Physics* **62**, 453 (2013), <https://doi.org/10.1080/00018732.2013.862020>.
- [63] N. Dupuis, L. Canet, A. Eichhorn, W. Metzner, J. Pawłowski, M. Tissier, and N. Wschebor, *Physics Reports* **910**, 1 (2021), the nonperturbative functional renormalization group and its applications.
- [64] J. Beyer, J. B. Profe, and L. Klebl, *The European Physical Journal B* **95**, 65 (2022).
- [65] A. Georges, G. Kotliar, W. Krauth, and M. J. Rozenberg, *Reviews of Modern Physics* **68**, 13 (1996).
- [66] U. Schollwöck, *Annals of physics* **326**, 96 (2011).
- [67] R. Orús, *Annals of physics* **349**, 117 (2014).
- [68] S. Carr, S. Fang, H. C. Po, A. Vishwanath, and E. Kaxiras, *Phys. Rev. Res.* **1**, 033072 (2019).
- [69] Z.-D. Song and B. A. Bernevig, *Physical review letters* **129**, 047601 (2022).
- [70] S. Carr, D. Massatt, S. B. Torrisi, P. Cazeaux, M. Luskin, and E. Kaxiras, *Physical Review B* **98**, 224102 (2018).
- [71] X.-W. Zhang, C. Wang, X. Liu, Y. Fan, T. Cao, and D. Xiao, *Nature Communications* **15**, 4223 (2024).
- [72] Y. Jia, J. Yu, J. Liu, J. Herzog-Arbeitman, Z. Qi, H. Pi, N. Regnault, H. Weng, B. A. Bernevig, and Q. Wu, *Physical Review B* **109**, 205121 (2024).
- [73] E. Thompson, K. T. Chu, F. Mesple, X.-W. Zhang, C. Hu, Y. Zhao, H. Park, J. Cai, E. Anderson, K. Watanabe, *et al.*, arXiv preprint arXiv:2405.19308 (2024).
- [74] Y. Liu, Y. Gu, T. Bao, N. Mao, C. Li, S. Jiang, L. Liu, D. Guan, Y. Li, H. Zheng, *et al.*, arXiv preprint arXiv:2406.19310 (2024).
- [75] “Supplementary Material available at [URL will be inserted by publisher] with a description of (i) the continuum model and its projection to the Wannier basis, (ii) the technical details of the FRG simulations, and (iii) the spin fluctuation RPA mechanism for superconductivity, including Refs. [?].”
- [76] N. Marzari, A. A. Mostofi, J. R. Yates, I. Souza, and D. Vanderbilt, *Rev. Mod. Phys.* **84**, 1419 (2012).
- [77] S. Carr, S. Fang, H. C. Po, A. Vishwanath, and E. Kaxiras, *Phys. Rev. Res.* **1**, 033072 (2019).
- [78] A. Fischer, L. Klebl, D. M. Kennes, and T. O. Wehling, arXiv preprint arXiv:2407.02576 (2024).
- [79] H. Pan, F. Wu, and S. Das Sarma, *Physical Review*

- Research **2**, 033087 (2020).
- [80] J. Zang, J. Wang, J. Cano, A. Georges, and A. J. Millis, *Physical Review X* **12**, 021064 (2022).
- [81] D. Kiese, Y. He, C. Hickey, A. Rubio, and D. M. Kennes, *APL Materials* **10** (2022).
- [82] M. Zegrodnik and A. Biborski, *Physical Review B* **108**, 064506 (2023).
- [83] J. Motruk, D. Rossi, D. A. Abanin, and L. Rademaker, *Physical Review Research* **5**, L022049 (2023).
- [84] J. Wang, J. Zang, J. Cano, and A. J. Millis, *Physical Review Research* **5**, L012005 (2023).
- [85] C. Husemann and M. Salmhofer, *Phys. Rev. B* **79**, 195125 (2009).
- [86] J. Lichtenstein, D. Sánchez de la Peña, D. Rohe, E. Di Napoli, C. Honerkamp, and S. Maier, *Computer Physics Communications* **213**, 100 (2017).
- [87] J. B. Profe and D. M. Kennes, *The European Physical Journal B* **95**, 60 (2022).
- [88] J. B. Profe, D. M. Kennes, and L. Klebl, *SciPost Phys. Codebases*, 26 (2024).
- [89] C. Honerkamp, *Physical Review B* **68**, 104510 (2003).
- [90] R. Nandkishore, L. S. Levitov, and A. V. Chubukov, *Nature Physics* **8**, 158 (2012).
- [91] A. M. Black-Schaffer and C. Honerkamp, *Journal of Physics: Condensed Matter* **26**, 423201 (2014).
- [92] L. Classen, C. Honerkamp, and M. M. Scherer, *Physical Review B* **99**, 195120 (2019).
- [93] M. M. Scherer, D. M. Kennes, and L. Classen, *npj Quantum Materials* **7**, 1 (2022).
- [94] A. P. Schnyder, S. Ryu, A. Furusaki, and A. W. W. Ludwig, *Phys. Rev. B* **78**, 195125 (2008).
- [95] T. Takimoto, T. Hotta, and K. Ueda, *Phys. Rev. B* **69**, 104504 (2004).
- [96] A. Fischer, L. Klebl, C. Honerkamp, and D. M. Kennes, *Physical Review B* **103**, L041103 (2021).
- [97] P. Mai, S. Karakuzu, G. Balduzzi, S. Johnston, and T. A. Maier, *Proceedings of the National Academy of Sciences* **119**, e2112806119 (2022).
- [98] F. Šimkovic IV, R. Rossi, and M. Ferrero, *Phys. Rev. Res.* **4**, 043201 (2022).
- [99] We foresee this scale-dependent nesting as a general feature of weak-to-moderately interacting fermions with HOVHS.

Supplementary Material:

Theory of intervalley-coherent AFM order and topological superconductivity in $tWSe_2$

Ammon Fischer,¹ Lennart Klebl,^{2,3} Valentin Crépel,⁴ Siheon Ryee,³ Angel Rubio,^{5,6} Lede Xian,^{7,8,5}
 Tim O. Wehling,^{3,9} Antoine Georges,^{10,4,11,12} Dante M. Kennes,^{1,5} and Andrew J. Millis^{4,13}

¹*Institute for Theory of Statistical Physics, RWTH Aachen University,
 and JARA Fundamentals of Future Information Technology, 52062 Aachen, Germany*

²*Institute for Theoretical Physics and Astrophysics and Würzburg-Dresden Cluster of Excellence ct.qmat,
 University of Würzburg, 97074 Würzburg, Germany*

³*I. Institute of Theoretical Physics, Universität Hamburg, Notkestraße 9-11, 22607 Hamburg, Germany*

⁴*Center for Computational Quantum Physics, Flatiron Institute, New York, NY 10010, USA*

⁵*Max Planck Institute for the Structure and Dynamics of Matter,
 Center for Free Electron Laser Science, 22761 Hamburg, Germany*

⁶*Center for Computational Quantum Physics, Simons Foundation Flatiron Institute, New York, NY 10010 USA*

⁷*Tsientang Institute for Advanced Study, Zhejiang 310024, China*

⁸*Songshan Lake Materials Laboratory, 523808 Dongguan, Guangdong, China*

⁹*The Hamburg Centre for Ultrafast Imaging, 22761 Hamburg, Germany*

¹⁰*Collège de France, 11 place Marcelin Berthelot, 75005 Paris, France*

¹¹*CPHT, CNRS, Ecole Polytechnique, Institut Polytechnique de Paris, Route de Saclay, 91128 Palaiseau, France*

¹²*DQMP, Université de Genève, 24 quai Ernest Ansermet, CH-1211 Genève, Suisse*

¹³*Department of Physics, Columbia University, 538 West 120th Street, New York, NY 10027, USA*

CONTENTS

I. Continuum model and Wannier projection	2
A. Continuum model parameters	2
B. Topology of the continuum model	2
C. Single-shot projection	2
D. Coulomb interactions	4
E. Other twist angles	6
II. Functional Renormalization Group	8
A. divERGE input parameters	9
B. Full momentum and orbital dependence of the IVC-AFM state and SC order parameter	9
C. FRG phase diagram including only nearest-neighbor repulsion terms	9
III. Random Phase Approximation	11
A. Flowing RPA	11
B. RPA mechanism for superconductivity	11
References	12

I. CONTINUUM MODEL AND WANNIER PROJECTION

A. Continuum model parameters

We employ the continuum model for tWSe₂ [1–3], which is a $\mathbf{k} \cdot \mathbf{p}$ expansion for the spin-valley locked states near the $K^{(l)}$ valleys of the two WSe₂ monolayers coupled by moiré potentials. Focusing on the spin sector coming from the K valley of the two monolayers, the continuum Hamiltonian as a matrix in layer space reads

$$H(\mathbf{k}) = \begin{pmatrix} (\mathbf{k} - \boldsymbol{\kappa})^2/2m^* + \Delta_+(\mathbf{r}) & T_M(\mathbf{r}) \\ T_M^\dagger(\mathbf{r}) & (\mathbf{k} - \boldsymbol{\kappa}')^2/2m^* + \Delta_-(\mathbf{r}) \end{pmatrix} + \begin{pmatrix} E_z & 0 \\ 0 & -E_z \end{pmatrix}, \quad (1)$$

with $m^* = 5.643 \cdot 10^{-5} (\text{\AA} \text{meV})^{-1}$ the hole effective mass, and E_z the transverse electric field. The $\boldsymbol{\kappa}$ and $\boldsymbol{\kappa}'$ points denote the position of the K -point coming from the top and bottom layers, respectively, which are slightly displaced due to the small twist. The intra- and inter-layer moiré couplings read [1]

$$\Delta_{\pm}(\mathbf{r}) = V \sum_{\mathbf{g} \in \mathcal{O}} V \cos(\mathbf{g} \cdot \mathbf{r} \pm \psi), \quad (2)$$

$$T_M(\mathbf{r}) = w (1 + e^{i\mathbf{g}_1 \cdot \mathbf{r}} + e^{i\mathbf{g}_2 \cdot \mathbf{r}}). \quad (3)$$

The parameters $V = 9 \text{ meV}$, $\psi = 128^\circ$, and $w = 18 \text{ meV}$ were obtained by Devakul *et al.* [2] by fitting Eq. (1) to large-scale *ab-initio* calculations at the commensurate twist angle $\theta = 5.08^\circ$. The ‘ \mathcal{O} ’ denotes the set of the first shell of moiré reciprocal lattice vectors, and $\mathbf{g}_{1,2}$ are two reciprocal lattice vectors in the first shell rotated by 60° with respect to each other.

The lattice is set up as follows: We use $\mathbf{a}_1 = (a, 0)^T$ and $\mathbf{a}_2 = a(1/2, \sqrt{3}/2)^T$ as primitive lattice vectors, where $a = 3.317 \text{ \AA}$ is the lattice constant of WSe₂. The reciprocal lattice vectors follow as $\hat{\mathbf{b}} = 2\pi(\hat{\mathbf{a}}^{-1})^T$ which are used to obtain the reciprocal moiré lattice vectors through $\mathbf{g}_0 = R(\theta/2)\mathbf{b}_1 - R(-\theta/2)\mathbf{b}_2$ [$R(\varphi)$ is a two-dimensional rotation matrix with angle φ ; and θ is the twist angle]. The other reciprocal lattice vectors in the first shell follow as $\mathbf{g}_n = R(n\pi/3)\mathbf{g}_0$. Real-space moiré lattice vectors are given by inversion of reciprocal lattice vectors, i.e., $\hat{\mathbf{A}} = 2\pi(\hat{\mathbf{g}}^{-1})^T$.

In order to setup the Hamiltonian, we go to reciprocal moiré lattice vector (\mathbf{g}) space instead of real-space. The expansion is truncated after 3 shells, which is sufficient for convergence of the three highest energy valence bands at the relatively large twist angles considered in our study.

B. Topology of the continuum model

In order to construct exponentially localized Wannier functions, we have to understand the topology of the first couple of bands in the continuum model. To calculate Berry’s curvature $\Omega_z(\mathbf{k})$, we employ a modified Fukui-Hatsugai algorithm [4], where we add momentum points *outside* the first Brillouin-zone (BZ), because the continuum model is *not* periodic in reciprocal space. Figure 1 displays $\Omega_z(\mathbf{k})$ for various values of E_z , clearly showing how not only the first, but all three high-energy valence bands are topologically nontrivial. Moreover, they do not form a subspace with zero total Chern number \mathcal{C} . As a consequence, more states than those originating from the three topmost bands have to be taken into account for the construction of a representation as exponentially localized orbitals.

C. Single-shot projection

As it is natural to discuss Wannierization in real space, we have to map the eigenvectors of the continuum Hamiltonian $H(\mathbf{k})_{\mathbf{g},\mathbf{g}'}$ [cf. Eq. (1)] to real space. The truncation in reciprocal moiré lattice vector space is formulated in terms of shells, so we have to make sure to add enough real-space positions inside the moiré unit cell to accommodate all \mathbf{g} -vectors. We ensure this by using a 9×9 regular real-space mesh inside the (rhombus shaped) moiré unit cell for the inverse Fourier transformation. We then set up the transformation matrix from \mathbf{g} - to \mathbf{r} -space:

$$U_{\mathbf{r},\mathbf{g}}^{1,2} = e^{-i\mathbf{r} \cdot \mathbf{g} + i\mathbf{r} \cdot \mathbf{K}^{1,2}}, \quad (4)$$

where $\mathbf{K}^{1,2}$ denotes the K -point of layer 1, 2.

For Wannierization, we setup a \mathbf{k} -mesh of 24×24 regularly spaced points in the BZ, which translates to a 24×24 moiré lattice vector mesh for the Wannier functions. We diagonalize the continuum Hamiltonian $H(\mathbf{k})$ on each \mathbf{k} -point, resulting in bands $\epsilon_b(\mathbf{k})$ and Bloch functions $U_{\mathbf{g},l,b}(\mathbf{k})$, with b a band index and l the layer index. The Bloch

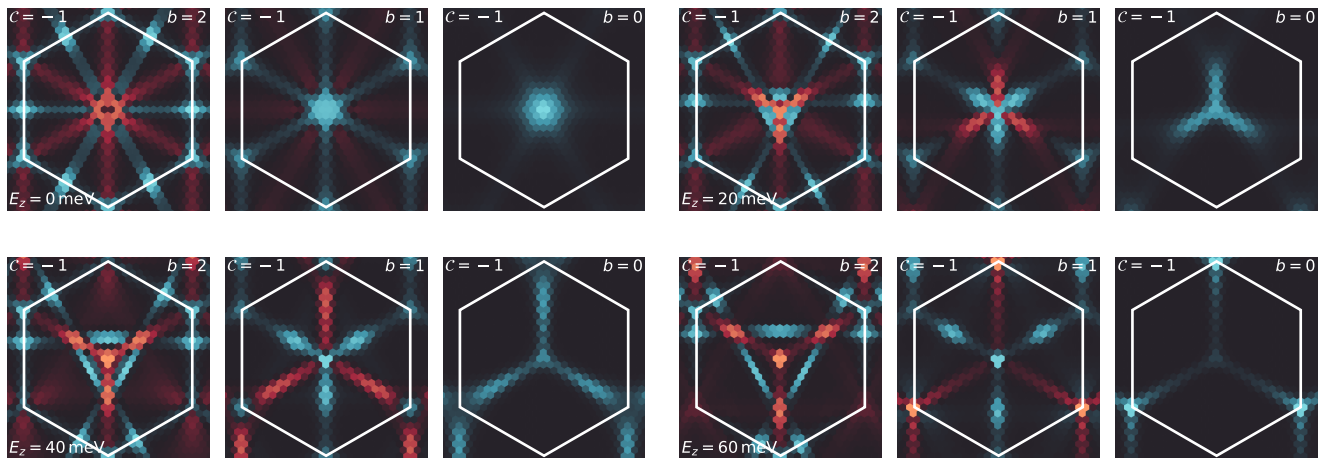


FIG. 1. Berry curvature of the continuum model at a twist angle of $\theta = 5.08^\circ$ for various values of displacement fields E_z . The Berry curvature $\Omega_z(\mathbf{k})$ of the top three valence bands ($b = 0$ denotes the valence band) is shown, with red/blue corresponding to positive/negative values; the colormap is centered around zero (black). In the top left corner of each panel, we indicate the Chern number \mathcal{C} of the corresponding band b . In 5.08° tWSe₂ (for the values of E_z shown, indicated in the lower left of each group of three panels next to each other), the first three valence bands consistently show $\mathcal{C} = -1$.

functions are transformed to “orbital” (\mathbf{r}) space using Eq. (4):

$$U_{\mathbf{r},l,b}(\mathbf{k}) = \sum_{\mathbf{g}} U_{\mathbf{r},\mathbf{g}}^l e^{-i\mathbf{k}\cdot\mathbf{r}} U_{\mathbf{g},l,b}(\mathbf{k}). \quad (5)$$

The trial Wannier functions $W^\xi(\mathbf{R} + \mathbf{r}, l)$, defined on the moiré lattice \mathbf{R} , the “orbital” positions \mathbf{r} , and layer l , are cast to reciprocal space using

$$W^\xi(\mathbf{k}, \mathbf{r}, l) = \sum_{\mathbf{R}} e^{i\mathbf{R}\cdot\mathbf{k}} W^\xi(\mathbf{R} + \mathbf{r}, l). \quad (6)$$

We then calculate the projection of W^ξ onto the Bloch states U :

$$\tilde{P}(\mathbf{k})_{\xi,b} = \sum_{\mathbf{r},l} W^\xi(\mathbf{k}, \mathbf{r}, l) U_{\mathbf{r},l,b}^*. \quad (7)$$

Following Refs. [5, 6], we apply an exponential weighting scheme to \tilde{P} in order to restrict the overlaps to a meaningful energy range:

$$P_{\xi,b}(\mathbf{k}) = e^{-|\epsilon_b(\mathbf{k})|/\eta} \tilde{P}_{\xi,b}(\mathbf{k}). \quad (8)$$

Here, the exponential decay width is set to $\eta = 80$ meV. We then perform a Löwdin orthonormalization of the overlaps and arrive at orthonormal Wannier functions [7]. Technically, the orthonormalization is implemented in a singular value decomposition:

$$\hat{P}(\mathbf{k}) = \hat{U}(\mathbf{k}) \hat{\Sigma}(\mathbf{k}) \hat{V}(\mathbf{k}), \quad (9)$$

$$\mathcal{W}^\xi(\mathbf{k}, \mathbf{r}, l) = \sum_b (\hat{U} \hat{V}^\dagger)_{\xi,b} e^{i\mathbf{k}\cdot\mathbf{r}} U_{\mathbf{r},l,b}(\mathbf{k}). \quad (10)$$

The orthonormal Wannier functions \mathcal{W} spread their spectral weight over more than the three first valence bands, given the non-trivial topology of this manifold in the continuum model. This is achieved by (i) projecting the trial states to all bands and (ii) introducing the exponential weighting factors in the projectors Eq. (8).

We choose our trial states according to the minimal model put forward in Ref. [8]: One s -orbital in the origin of the unit cell, on the triangular site (T -orbital), and two p_+ (p_- in the other valley) orbitals on the honeycomb sites ($H_{1,2}$ -orbitals)—the orbital index ξ can therefore take the values $\xi \in \{T, H_1, H_2\}$. We supplement the orbital character with gaussian envelopes of width $\sigma = 0.2|\mathbf{A}|$. Notably, the honeycomb orbitals are layer-polarized, i.e., the H_1 -orbital (H_2 -orbital) resides purely in layer 1 (0; cf. Fig. 1 (b) of the main text). The phase- and amplitude real-space profiles of the orthogonal Wannier functions \mathcal{W}^ξ for various values of E_z are shown in Fig. 2, the band structures are shown in Fig. 3, and the Berry curvature in Fig. 4. We show how the band structure converges as a function of the maximum hopping distance taken into account in the wannier model in Fig. 5.

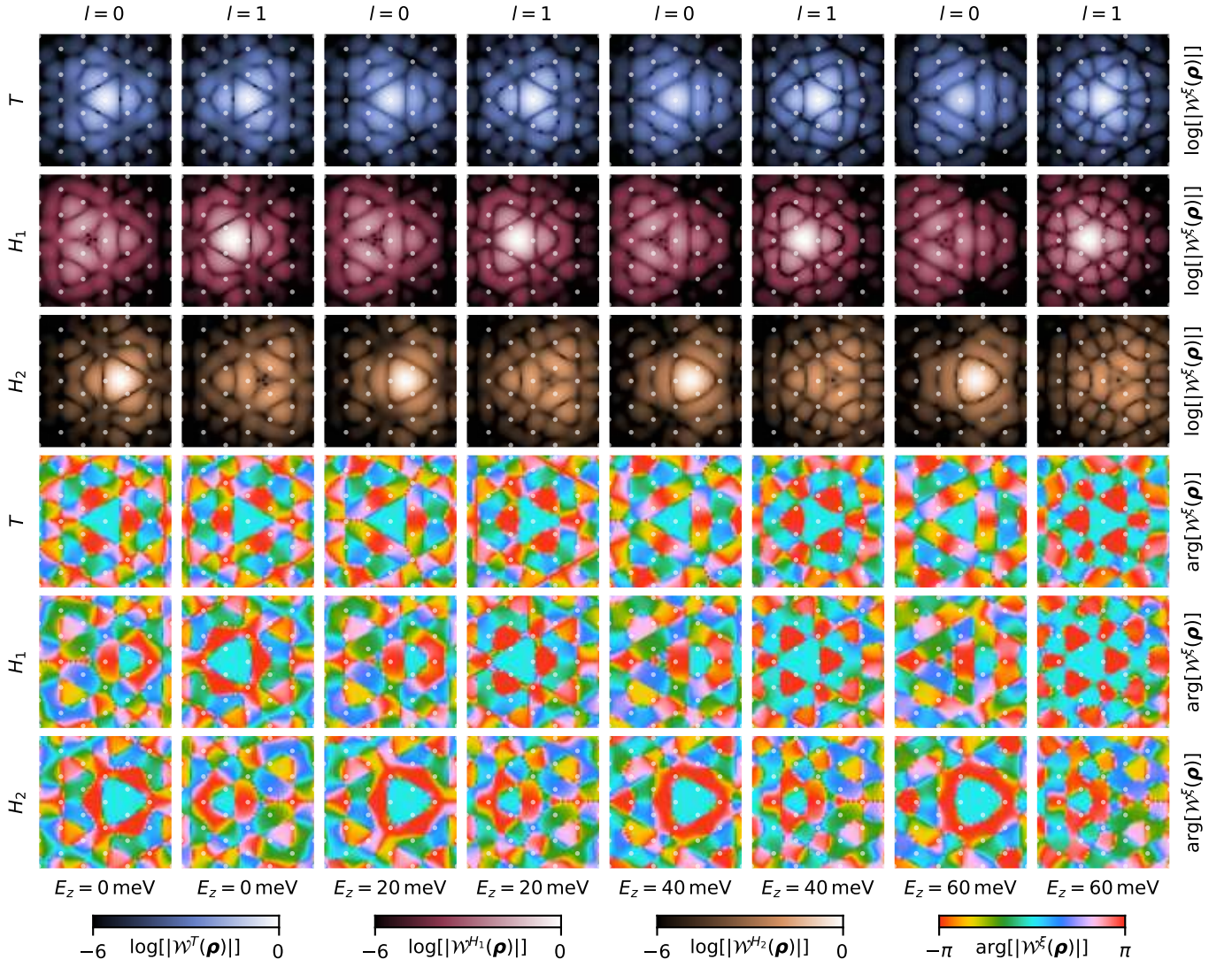


FIG. 2. Real-space amplitude (upper three rows) and phase (lower three rows) of the Wannier functions $\mathcal{W}^\xi(\boldsymbol{\rho})$. Each group of two subsequent columns correspond to a different displacement field E_z , with the layer index l altering within the group. The rows correspond to the orbitals T , H_1 , and H_2 .

D. Coulomb interactions

We denote the real-space Wannier functions centered around a moiré lattice site \mathbf{R} as $\mathcal{W}_{\mathbf{R}}^{\nu\xi}(\boldsymbol{\rho}) \equiv \mathcal{W}^{\nu\xi}(\boldsymbol{\rho} - \mathbf{R} + l)$, where ν is the spin/valley sector. With these, we can formulate Coulomb integrals to project the two-particle density-density interaction operator onto the Wannier model. Since the Coulomb interaction inherently operates on different spins, we first have to construct the time-reversal partners $\mathcal{W}^{\bar{\nu},\xi} = \mathcal{T}\mathcal{W}^{\nu\xi} = (\mathcal{W}^{\nu\xi})^*$. All nonzero Coulomb integrals then read

$$V_{(\nu_1, \xi_1) \dots (\nu_4, \xi_4)}^{\mathbf{R}_1, \mathbf{R}_2, \mathbf{R}_3, \mathbf{R}_4} = \sum_{\boldsymbol{\rho}, \boldsymbol{\rho}'} (\mathcal{W}_{\mathbf{R}_1}^{\nu_1 \xi_1}(\boldsymbol{\rho}) \mathcal{W}_{\mathbf{R}_2}^{\nu_2 \xi_2}(\boldsymbol{\rho}'))^* \mathcal{W}_{\mathbf{R}_3}^{\nu_3 \xi_3}(\boldsymbol{\rho}) \mathcal{W}_{\mathbf{R}_4}^{\nu_4 \xi_4}(\boldsymbol{\rho}') V(|\boldsymbol{\rho} - \boldsymbol{\rho}'|) \delta_{\nu_1, \nu_3} \delta_{\nu_2, \nu_4}, \quad (11)$$

with the sum over $\boldsymbol{\rho}$ running over all real-space positions. i.e, moiré lattice vectors \mathbf{R} , intra-cell positions \mathbf{r} , and layers l . For the interaction profile $V(r)$, we employ an experimentally motivated dual-gated Coulomb interaction [9], with short-range divergencies regularized with an Ohno form [6]:

$$V(r) = 4V_0 \sum_{k=0}^{\infty} K_0 \left[(2k+1)\pi \frac{\sqrt{r^2 + a^2}}{\xi} \right]. \quad (12)$$

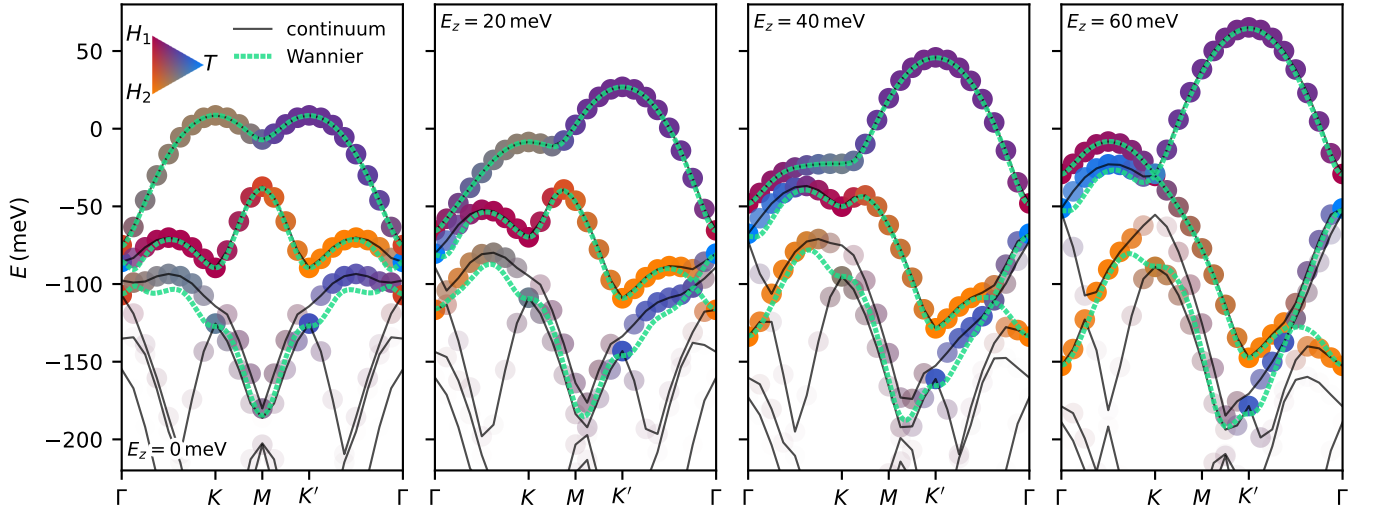


FIG. 3. Band structures of the Wannier model compared to the continuum model for $\theta = 5.08^\circ$ and several values of E_z . The overlap as well as the orbital content is included as color in the continuum band structure, while the Wannier band structure is given in cyan.

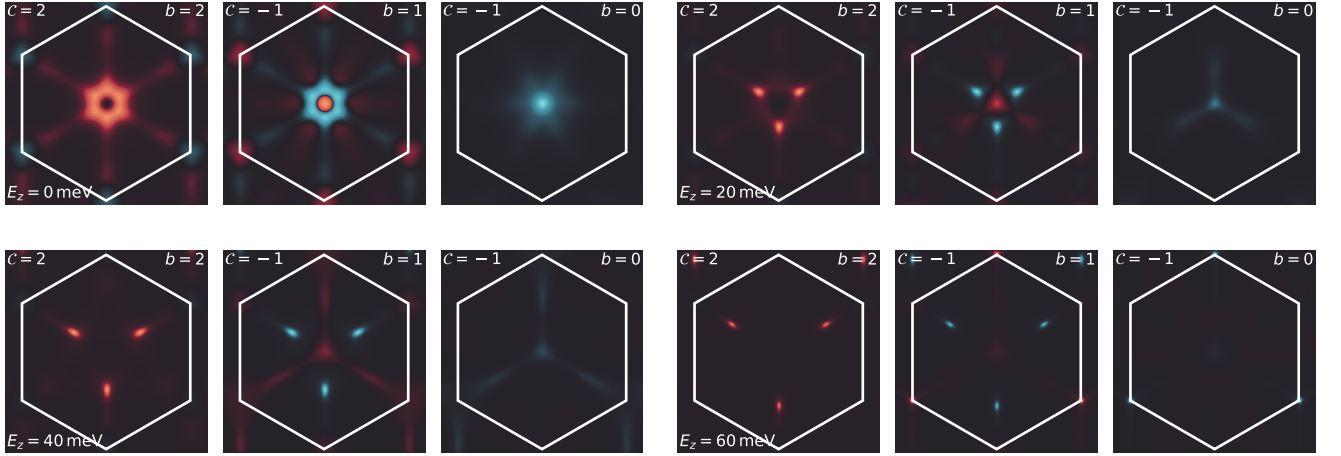


FIG. 4. Berry curvature for the three-band Wannier model of tWSe₂ at $\theta = 5.98^\circ$ at various values of displacement field E_z . Each panel corresponds to a given band b (counted from high to low energies, indicated in the top right corner) and displacement field E_z (indicated in the bottom left corner for each group of three panels). The Chern number C is given in the top left corner. The colormap is symmetric around zero (black), and positive (negative) values are red (blue). Comparing with Fig. 1, we observe that the topology of the first band is reproduced perfectly, while the second- and third bands display a mismatch. This is expected behavior, as the topmost three bands of the continuum model do not form a topologically trivial subspace.

Here, K_0 denotes a modified Bessel function of the second kind and ξ is the distance from the sample to either gate. The interaction parameters V_0 , a are related to physical parameters as follows:

$$a = \frac{\alpha}{\epsilon U}, \quad V_0 = \frac{a}{\epsilon \xi}, \quad (13)$$

with ϵ the dielectric constant of the sample's environment, α the fine structure constant, and U the on-site interaction strength.

For the calculation of interaction parameters in $\theta = 5.08^\circ$ tWSe₂, we use $U = 3$ eV, and the experimentally motivated $\xi = 100$ Å, and $\epsilon = 16$. The Wannier function spread is of the same order of magnitude as the screening length ξ , which yields dominant short-ranged interactions. Figure 6 displays the density-density interaction parameters (where $\mathbf{R}_1 = \mathbf{R}_3$, $\mathbf{R}_2 = \mathbf{R}_4$, $\xi_1 = \xi_3$, $\xi_2 = \xi_4$) as a function of distance for all orbital combinations (i.e. T - T , T - H , and H - H). Since nonzero displacement field E_z only slightly changes the shape of the Wannier functions, we assume

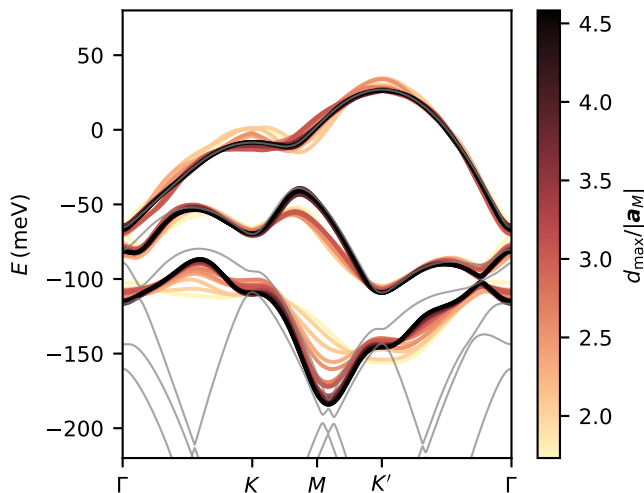


FIG. 5. Wannier dispersion for $\theta = 5.08^\circ$ and $E_z = 20$ meV for several values of the maximum hopping distance d_{\max} in units of the moiré lattice constant $|\mathbf{a}_M|$. The continuum band structure is plotted in gray. We observe that for $d_{\max} \gtrsim 3.5 \mathbf{a}_M$, the bands are well converged.

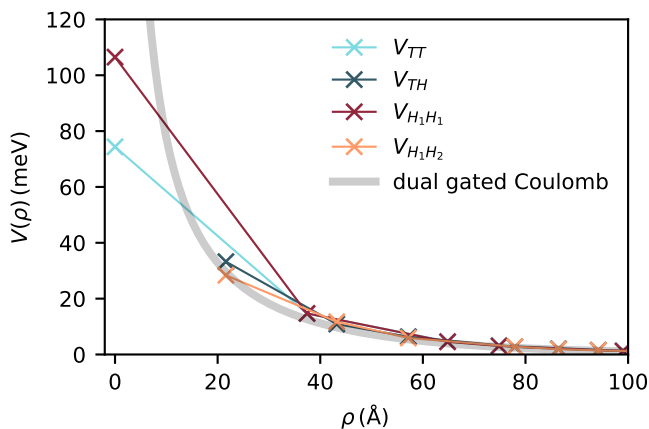


FIG. 6. Density-density interactions in the Wannier basis as a function of distance ρ between Wannier centers for $\theta = 5.08^\circ$, and the dual-gated Coulomb interaction given in Eq. (12). All interactions beyond nearest neighbors collapse onto a single line. In addition to the Wannier projected vertex elements, we plot the bare dual-gated Coulomb interaction (thick gray line), which falls on top of the vertex elements in the Wannier basis for large distances, signaling that the Coulomb/gate tail is reached.

the interaction parameters to be independent of E_z . We also calculate nearest-neighbor exchange- and pair-hopping interactions, which are suppressed by a factor > 10 given the nontrivial Wyckoff positions of each of the orbitals. The density-density interaction parameters for all twist angles considered in the scope of this work (cf. Section IE) are summarized in Table I.

E. Other twist angles

In addition to the twist angle $\theta = 5.08^\circ$, we perform simulations for $\theta = 4.5^\circ$ and $\theta = 4.1^\circ$. The model parameters remain the same (cf. Section IA) except for the twist angle (which also changes the moiré lattice vectors & -constant). Figure 7 displays the band structure, overlaps, and Wannier functions for $\theta = 4.5^\circ$ and $\theta = 4.1^\circ$. As expected for tWSe₂, the band structure flattens continuously with decreasing θ . The most important interaction parameters are summarized in Table I. Nearest-neighbor exchange- and pair-hopping terms are all smaller than 7 meV.

We further provide the density of states (DOS) as function of (hole) filling per moiré unit cell n/n_0 and external displacement field E_z for the set of Wannier functions obtained for $\theta = \{5.1^\circ, 4.5^\circ, 4.1^\circ\}$ (see Fig. 8). The position of the higher-order van-Hove singularity is indicated by the blue circle and stands out due the enhanced DOS (visualized by the colorbar).

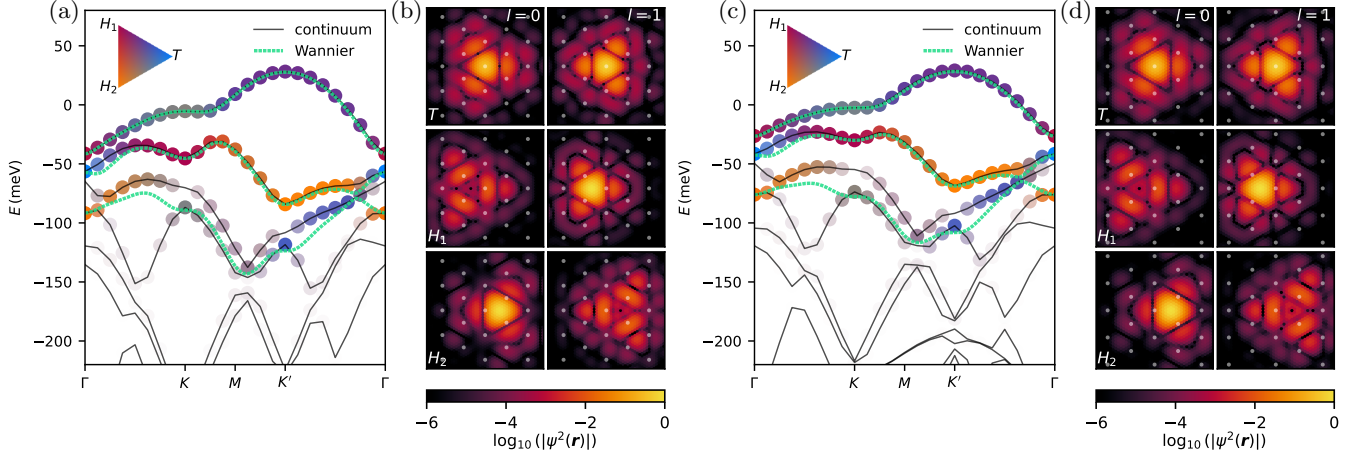


FIG. 7. Band structure (a,c) and Wannier functions (b,d) for tWSe₂ at $\theta = 4.5^\circ$ (a,b) and $\theta = 4.1^\circ$ (c,d). In all panels, we set $E_z = 20$ meV. Panels (a,c) contain the continuum model band structures (black), the Wannier model band structures (cyan) and the overlap of the Wannier functions to the continuum model Bloch states (colored dots). The amplitude of the Wannier functions (b,d) is shown on a logarithmic scale, highlighting its exponential decay outside the first unit cell. The moiré lattice vectors are shown as faint white dots.

TABLE I. Interaction parameters in the Wannier model for several twist angles. $U_{T,H}$ denote Hubbard interactions on T - and H -orbitals, and $V_{TH,HH}$ correspond to nearest-neighbor density-density repulsion on T - H - and H - H -bonds (cf. main text).

θ	U_T (meV)	U_H (meV)	V_{TH} (meV)	V_{HH} (meV)
4.1°	74.4	113.2	26.7	22.5
4.5°	74.3	109.9	29.5	25.0
5.08°	74.4	106.5	33.3	28.4

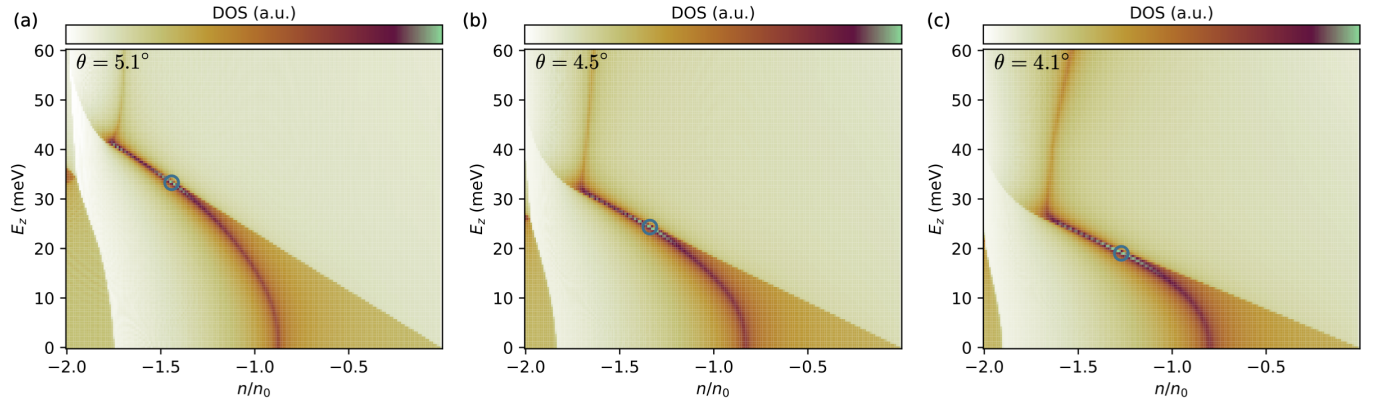


FIG. 8. Density of states as function of (hole) filling per moiré unit cell n/n_0 and external displacement field E_z for tWSe₂ at twist angles (a) $\theta = 5.1^\circ$ (b) $\theta = 4.5^\circ$ and (c) $\theta = 4.1^\circ$. The position of the higher order van-Hove singularity is indicated by the blue circle.

II. FUNCTIONAL RENORMALIZATION GROUP

The functional renormalization group (FRG) [10–14] represents a well-established method to predict particle-particle and particle-hole instabilities in an unbiased manner in the weak-to-moderate coupling regime. FRG smoothly connects the non-interacting action to the interacting one by virtue of a renormalization group (RG) scale $\Lambda = \infty \rightarrow 0$. The introduction of the RG scale leads to an infinite hierarchy of coupled differential equations for the vertex functions $\Gamma^{(2n)}$. In order to numerically tackle the problem, we must truncate the hierarchy and approximate the vertex functions' dependencies. We here employ the common truncation at the two-particle vertex $\Gamma^{(4)}$, and furthermore ignore self-energies, i.e., $\Gamma^{(2)} \equiv 0$. In addition, we approximate $\Gamma^{(4)}$ as a static quantity, disregarding its dependency on Matsubara frequencies. Within the framework of static four-point FRG, we employ the truncated unity (TUFGR) approximation [15–17], which compresses secondary momentum dependencies (those not corresponding to the Mandelstam variable of a given diagrammatic channel) of $\Gamma^{(4)}$ by inserting truncated lattice Fourier transformations. In static four-point FRG, the onset of an ordered phase is signaled by the divergence of the two-particle vertex $\Gamma^{(4)}$ at a particular (critical) scale Λ_c . The most divergent eigenvalue (and the accompanying eigenvector) of $\Gamma^{(4)}$ then provides insights into the structure of the ordered phase—whether it is a particle-particle or a particle-hole instability, and e.g. the momentum, spin/valley, and orbital structure of the order parameter. Since we choose the sharp frequency cutoff as regulator (as implemented in the divERGE library [18]), the critical scale Λ_c serves as a proxy for the critical temperature of the transition. The FRG flow equations for the vertex Γ^Λ and its decomposition into the three diagrammatic channels P^Λ , C^Λ , and D^Λ read (see Fig. 9 for a diagrammatic representation)

$$\frac{d}{d\Lambda} \Gamma^\Lambda = \frac{d}{d\Lambda} P^{-1}[P^\Lambda] + \frac{d}{d\Lambda} C^{-1}[C^\Lambda] + \frac{d}{d\Lambda} D^{-1}[D^\Lambda], \quad (14)$$

$$\frac{d}{d\Lambda} P_{a_1 a_2}^\Lambda(\mathbf{q}_P, \mathbf{k}_P, \mathbf{k}'_P) = \frac{1}{2} P[\Gamma^\Lambda]_{a_3' a_4'}^{a_1 a_2}(\mathbf{q}_P, \mathbf{k}_P, \mathbf{k}) \dot{L}_{a_3' a_4'}^{-, \Lambda}(\mathbf{q}_P, \mathbf{k}) P[\Gamma^\Lambda]_{a_3 a_4}^{a_1' a_2'}(\mathbf{q}_P, \mathbf{k}, \mathbf{k}'_P), \quad (15)$$

$$\frac{d}{d\Lambda} D_{a_3 a_4}^\Lambda(\mathbf{q}_D, \mathbf{k}_D, \mathbf{k}'_D) = -D[\Gamma^\Lambda]_{a_3' a_4'}^{a_1 a_2}(\mathbf{q}_D, \mathbf{k}_D, \mathbf{k}) \dot{L}_{a_3' a_4'}^{+, \Lambda}(\mathbf{q}_D, \mathbf{k}) D[\Gamma^\Lambda]_{a_3 a_4}^{a_1' a_2'}(\mathbf{q}_D, \mathbf{k}, \mathbf{k}'_D), \quad (16)$$

$$\frac{d}{d\Lambda} C^{-1}[C^\Lambda]_{a_1 a_2}(\mathbf{k}_1, \mathbf{k}_2, \mathbf{k}_3) = -\frac{d}{d\Lambda} D^{-1}[D^\Lambda]_{a_4 a_3}^{a_1 a_2}(\mathbf{k}_1, \mathbf{k}_2, \mathbf{k}_1 + \mathbf{k}_2 - \mathbf{k}_3), \quad (17)$$

where we do not make the form factor expansion (the ‘truncated unities’) explicit but constrain ourselves to the full orbital-momentum space formulation in which further $\mathbf{a} = (o, s)$ encodes the orbital and spin-valley degrees of freedom. The operator $X^{(-1)}[Y^\Lambda]$ describes a cross-channel projection from vertex Y^Λ into (out of) channel $X \in \{P, C, D\}$ and all multiply occurring indices are summed over. For an introduction into TUFGR, we refer the reader to Refs. [14–16] and especially Ref. [17]. Using a sharp frequency cutoff as regulator allows to efficiently evaluate the loop integrals $\dot{L}^{\pm, \Lambda}$ by virtue of convolutions in the momentum domain

$$\dot{L}_{a_3 a_4}^{-, \Lambda}(\mathbf{q}, \mathbf{k}) = \frac{d}{d\Lambda} \int \frac{dk_0}{2\pi} G_{a_1 a_3}^\Lambda(k_0, \mathbf{k}) G_{a_2 a_4}^\Lambda(-k_0, -\mathbf{k} + \mathbf{q}) = \frac{1}{2\pi} [G_{a_1 a_3}^0(\Lambda, \mathbf{k}) G_{a_2 a_4}^0(-\Lambda, -\mathbf{k} + \mathbf{q}) + \text{h.c.}], \quad (18)$$

$$\dot{L}_{a_3 a_4}^{+, \Lambda}(\mathbf{q}, \mathbf{k}) = \frac{d}{d\Lambda} \int \frac{dk_0}{2\pi} G_{a_2 a_3}^\Lambda(k_0, \mathbf{k}) G_{a_4 a_1}^\Lambda(+k_0, +\mathbf{k} - \mathbf{q}) = \frac{1}{2\pi} [G_{a_2 a_3}^0(\Lambda, \mathbf{k}) G_{a_4 a_1}^0(+\Lambda, +\mathbf{k} - \mathbf{q}) + \text{h.c.}]. \quad (19)$$

Here, $\hat{G}^0(k_0, \mathbf{k}) = [ik_0 - \hat{H}(\mathbf{k})]^{-1}$ is the bare propagator written in the basis of the spin/orbital degrees of freedom as indicated by the hat symbol. Using a sharp frequency cutoff, the regularized propagator reads $\hat{G}^\Lambda(k_0, \mathbf{k}) = \theta(|k_0| - \Lambda) \hat{G}^0(k_0, \mathbf{k})$ and the derivative in Eq. (19) is evaluated by virtue of Morris Lemma [11].

To gain information about the momentum, spin-valley and orbital structure of the leading order parameter that is signaled by a divergence of $\Gamma^{(4)}$, we compute two-particle Green's functions using the effective two-particle interaction vertex Γ^{Λ_c} at the critical scale Λ_c . To this end, the channel-specific two-particle Green's functions χ^X , $X \in \{P, C, D\}$ describe the response of fermionic bilinears of pairing, charge and spin type and can be cast into a series of generalized tensor contractions in analogue to Eq. (14) that reads

$$\chi_{a_3 a_4}^X(\mathbf{q}_X, \mathbf{k}_X, \mathbf{k}'_X) = \chi_{a_3' a_4'}^{\xi, \Lambda_c}(\mathbf{q}_X, \mathbf{k}_X) X[\Gamma^{\Lambda_c}]_{a_3' a_4'}^{a_1 a_2}(\mathbf{q}_X, \mathbf{k}_X, \mathbf{k}'_X) \chi_{a_3 a_4}^{\xi, \Lambda_c}(\mathbf{q}_X, \mathbf{k}'_X), \quad (20)$$

where $\xi = \pm$ in the P -channel (C/D -channel). The non-interacting two-particle Green's functions χ^{ξ, Λ_c} at scale Λ_c are obtained by integrating the non-interacting particle-particle (particle-hole) loop integrals $\dot{L}^{\pm, \Lambda}$ down to the critical scale Λ_c

$$\chi^{\xi, \Lambda_c}(\mathbf{q}_X, \mathbf{k}_X) = \int_{\Lambda_c}^{\infty} d\Lambda \dot{L}^{\xi, \Lambda}(\mathbf{q}_X, \mathbf{k}_X). \quad (21)$$

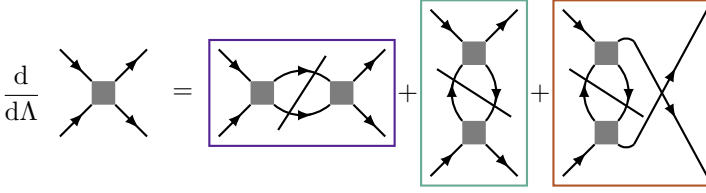


FIG. 9. Diagrammatic representation of the non- $SU(2)$ symmetric FRG flow equations of the four-point vertex $\Gamma^{(4)}$. The interaction is decomposed into two-particle reducible interaction channels including the particle-particle (blue), direct particle-hole (green) and crossed particle-hole (orange) channel. The slashed loops indicate the single-scale propagator.

Within TUFGR, the dependence of the interacting two-particle susceptibility defined in Eq. (22) on fermionic momenta can again be expanded in a form-factor basis to control the numerical complexity. Due to the U_ν -symmetry of the normal-state Hamiltonian, the transverse particle-hole susceptibility $\chi_{\uparrow\downarrow\uparrow\downarrow}^{\text{FRG}}$ is of particular interest as it describes the response of local particle-hole pairs from opposite spin-valley sectors and is given by the correlation function

$$\chi_{\uparrow\downarrow\uparrow\downarrow}^{\text{FRG}}(\mathbf{q}_C) = \sum_{\mathbf{k}_C, \mathbf{k}'_C} \chi_{\mathbf{a}_1\mathbf{a}_2}^C(\mathbf{q}_C, \mathbf{k}_C, \mathbf{k}'_C) \delta_{o_1 o_2} \delta_{o_3 o_4} \delta_{s_1\uparrow} \delta_{s_2\downarrow} \delta_{s_3\uparrow} \delta_{s_4\downarrow}, \quad (22)$$

where indices are arranged in channel-native ordering for the crossed particle-hole channel (1432).

To extract the particle-hole susceptibility $\chi_{\uparrow\downarrow\uparrow\downarrow}^{\text{FRG}}(\mathbf{q}_C)$ in the superconducting phase as shown in Fig. 2 (b) in the main text for $E_z < 25$ meV, we stop the flow just before reaching the divergence in the P -channel at scale $\tilde{\Lambda}_c \lesssim \Lambda_c$ such to avoid spurious contributions that stem from cross-channel projections of the divergent P -channel.

A. divERGE input parameters

The FRG calculations are carried out with the TUFGR backend of the divERGE code base [18]. The FRG flow equations (14) are solved using an adaptive Euler integrator using the parameters $\{\Lambda_0, \Lambda_{\text{min}}, d\Lambda_{\text{min}}, V_{\text{max}}\} = \{10^3, 10^{-2}, 10^{-3}, 10^4\}$ meV and $\{d\Lambda_{\text{fac}}, \Lambda_{\text{fac-scale}}\} = \{0.05, 10\}$. An extensive definition of above parameters is found in Ref. [18]. The form factor expansion of the (slow) fermionic momenta $(\mathbf{k}_X, \mathbf{k}'_X)$ is cut off at a distance of $2.01 |\mathbf{a}_M|$ including 129 form factors per spin in the parametrization of the vertex tensors. The bosonic momentum variable in each channel is resolved on a discrete mesh of $N_{\mathbf{k}} = 30 \times 30$ momentum points in the Brillouin zone. An additional $N_{\mathbf{k}_f} = 30 \times 30$ fine momentum mesh (for each coarse momentum point) is added to resolve the single-particle dispersion entering the (scaled) two-particle propagators $\tilde{L}^{\text{pp,ph}}$.

B. Full momentum and orbital dependence of the IVC-AFM state and SC order parameter

Besides the leading momentum transfer of the transverse particle-hole susceptibility $\chi_{\uparrow\downarrow\uparrow\downarrow}^{\text{FRG}}(\mathbf{q})$ extracted from the FRG analysis, we here provide information of the full momentum and Wannier orbital dependence as well as their phase dependence as shown in Fig. 11. As argued in the main text, the susceptibility along the van-Hove line has only notable weight between Wannier orbitals that shape the Fermi surface near the K^ν -points, i.e. T/H_2 . Meanwhile, contributions involving Bloch states with weight on the H_1 -orbital are suppressed. As we detune the system from the higher-order VHS (but staying on the van-Hove line, green arrow), the leading momentum transfer \mathbf{Q}_C , i.e. the maximum of $\chi_{\uparrow\downarrow\uparrow\downarrow}^{\text{FRG}}(\mathbf{q})$, moves towards the M -point. This indicates the commensurate-incommensurate transition that eventually stabilizes superconducting order on the van-Hove line.

C. FRG phase diagram including only nearest-neighbor repulsion terms

Besides the analysis of long-ranged density-density type interactions presented in the main text, we here resolve the FRG phase diagram at $\theta = 5.08^\circ$ including only the nearest-neighbor repulsion terms between the triangular (T) and honeycomb (H_1, H_2) sites

$$H^V = H + V_{TH} \sum_{\nu, \mu} \sum_{H \in \{H_1, H_2\}} \sum_{\langle \mathbf{R}, \mathbf{R}' \rangle} n_{\mathbf{R}H}^\nu n_{\mathbf{R}'T}^\mu + V_{HH} \sum_{\nu, \mu} \sum_{H \in \{H_1, H_2\}} \sum_{\langle \mathbf{R}, \mathbf{R}' \rangle} n_{\mathbf{R}H}^\nu n_{\mathbf{R}'\bar{H}}^\mu, \quad (23)$$

where the values of the nearest-neighbor honeycomb-triangular (honeycomb-honeycomb) density-density interaction $V_{TH} \approx 33$ meV ($V_{HH} \approx 28$ meV) are obtained from downfolding of the dual-gated Coulomb interaction to the Wannier

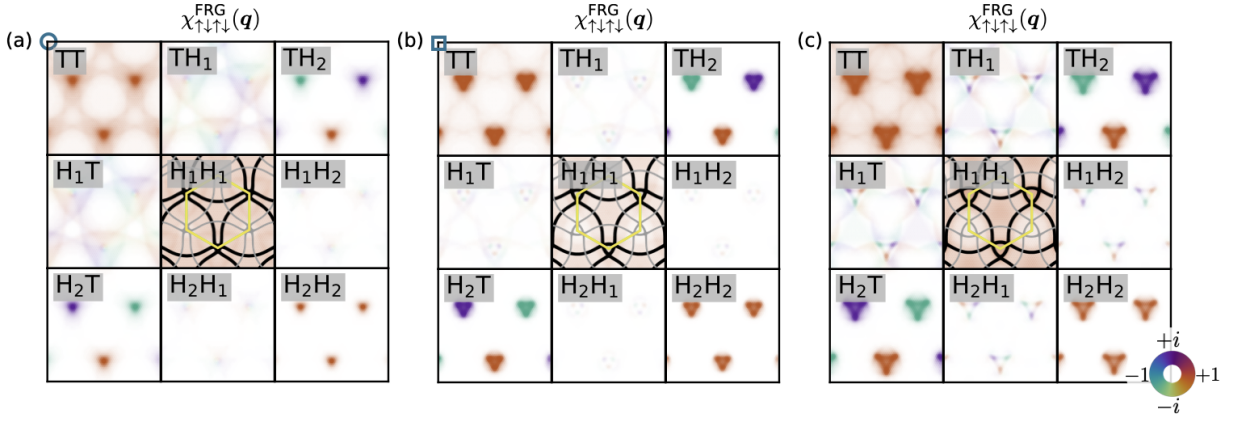


FIG. 10. Full momentum-orbital dependence of the particle-hole susceptibility $\chi_{\uparrow\downarrow\uparrow\downarrow}^{\text{FRG}}(\mathbf{q})$ evaluated at the end of the FRG flow at scale Λ_c . The relative phase (amplitude) of the susceptibility is encoded by the continuous colorbar (opacity). The three panels show the particle-hole susceptibility along the van-Hove line at displacement field strengths of $E_z = 33$ meV (a), $E_z = 25$ meV (b) and $E_z = 21$ meV (c). Detuning the system from the higher-order VHS (blue circle), shifts the leading momentum transfer, i.e. $\max_{\mathbf{q}} \chi_{\uparrow\downarrow\uparrow\downarrow}^{\text{FRG}}(\mathbf{q})$, from K^ν towards the M -point.

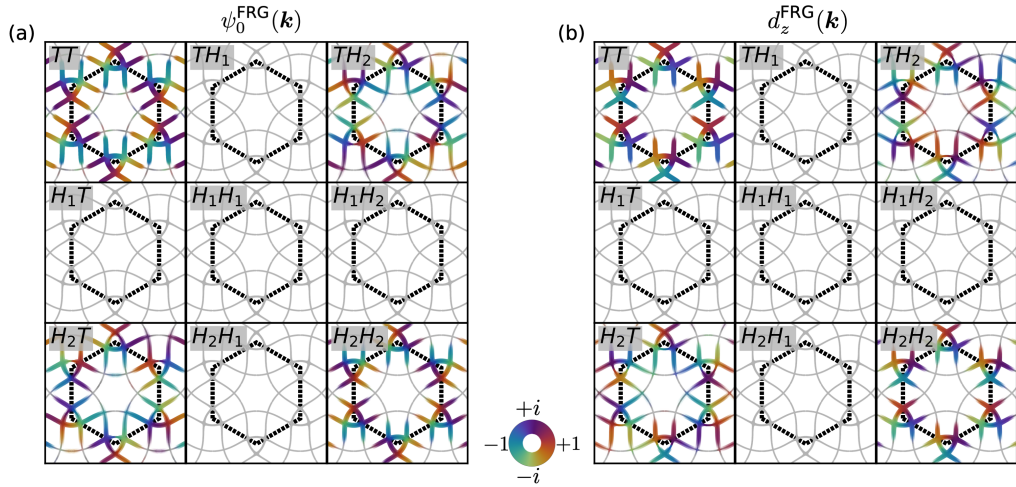


FIG. 11. Full momentum-orbital dependence of the leading superconducting order parameter $\Delta^{\text{SC}}(\mathbf{k})$ at $E_z = 25$ meV on the van-Hove line (blue square) extracted from the FRG analysis. The relative phase (amplitude) of the susceptibility is encoded by the continuous colorbar (opacity). The two panels show the SC order parameter decomposed into singlet $\psi_0^{\text{FRG}}(\mathbf{k})$ and triplet $d_z^{\text{FRG}}(\mathbf{k})$ components. The SC order parameter is two-fold degenerate and likely minimizes its free energy by the chiral superposition $d + id/p + ip$. Its amplitude is only notable for orbital combinations involving the Wannier orbitals (T, H_2), consistent with the structure of the particle-hole susceptibility $\chi_{\uparrow\downarrow\uparrow\downarrow}^{\text{FRG}}(\mathbf{q})$.

basis and the sum over $\langle \mathbf{R}, \mathbf{R}' \rangle$ includes nearest neighbor lattice vectors that imply actual nearest-neighbor T - H (H - H) bonds. The resulting FRG phase diagram is shown in Fig. 12 (a). In agreement with the phase diagram obtained when accounting for the entire distance dependence of density-density interactions presented in the manuscript, the IVC-AFM phase admixed with a non-local spin/valley-bond order (SBO) that is facilitated by the nearest-neighbor repulsion between triangular (T) and honeycomb (H_2) orbitals

$$\bar{\Delta}_{\mathbf{R}, \mathbf{R}'}^{\text{SBO}} \propto e^{i\mathbf{Q}_C \cdot \mathbf{R}} \langle c_{\mathbf{R}, T}^{\nu\dagger} \bar{\sigma}^{\nu\nu'} c_{\mathbf{R}', H_2}^{\nu'} \rangle + \text{h.c.} \quad (24)$$

This raises the critical scale of the particle-hole instability along the van-Hove line. Due to its symmetry-allowed coupling to the IVC-AFM phase, this also enlarges the regions of SC order in the phase diagram and the associated critical scale of the superconducting transition. The gain in free energy achieved by the formation of non-local vs. local particle-hole pairs is caused by the bare nearest-neighbor repulsion $V_{TH(HH)}$. Its projection in the crossed particle-hole channel, its expectation value with the SBO order parameter lowers the energy, favoring the spin-bond

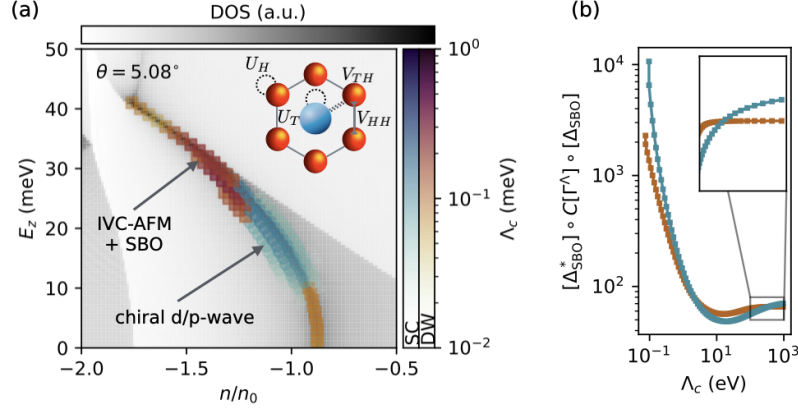


FIG. 12. FRG phase diagram in the presence of nearest-neighbor density-density interactions. (a) FRG phase diagram at $\theta = 5.08^\circ$ including the nearest-neighbor honeycomb-triangular (honeycomb-honeycomb) density-density interaction $V_{TH} \approx 33$ meV ($V_{HH} \approx 28$ meV). (b) Projection of the SBO bond order parameter onto the effective vertex in the crossed particle-hole channel $C[\Gamma^\Lambda]$ during the FRG flow. The red (blue) curve correspond to the case without (with) the nearest-neighbor repulsion terms $V_{TT,TH}$. The raise in the critical scale and the extension of SC regions in the phase diagram are tied to the formation of spin/valley bond order (SBO) that couples to the IVC-AFM state.

order parameter

$$\Delta^{\text{SBO}*} \circ C[\Gamma_{\Lambda=\infty}^{(4)}] \circ \Delta^{\text{SBO}} > 0. \quad (25)$$

Figure 12 (b) shows an exemplary FRG flow at $E_z = 29$ meV and $n/n_0 = -1.3$ with (without) nearest-neighbor interactions, underlining the above statement.

III. RANDOM PHASE APPROXIMATION

A. Flowing RPA

The non-interacting particle-particle (particle-hole) susceptibility $\chi^{0,\pm}(\mathbf{q}_X)$, $X \in \{P, C\}$ is calculated using the 'flowing' RPA formulation presented in Ref. [19], i.e. rewriting the Matsubara summation inherent to the two-particle propagator in the particle-hole (particle-particle) channel in terms of a Λ -flow with sharp frequency cutoff down to the desired temperature $T = \Lambda_{\min}$

$$\chi_{a_3 a_4}^{0,\pm}(\mathbf{q}_X) = \int_T^\infty d\Lambda \dot{L}_{a_1 a_2}^{\pm, \Lambda}(\mathbf{q}_C) = \int_T^\infty \frac{d\Lambda}{2\pi} \left[\frac{1}{N_{\mathbf{k}}} \sum_{\mathbf{k}} \underbrace{G_{a_1 a_4}^0(i\Lambda, \mathbf{k}) G_{a_2 a_3}^0(\pm i\Lambda, \pm \mathbf{k} \mp \mathbf{q}_X)}_{\chi_{a_3 a_4}^{\Lambda, \pm}(\mathbf{q}_X, \mathbf{k})} + \text{h.c.} \right]. \quad (26)$$

The effective RPA vertex in the crossed particle-hole channel is then given by the geometric series

$$\begin{aligned} C_{a_3 a_4}^{\text{RPA}}(\mathbf{q}_C) &= C[\Gamma^0]_{a_3 a_4}(\mathbf{q}_C) + C[\Gamma^0]_{a_3' a_4'}(\mathbf{q}_C) \chi_{a_1' a_2'}^{0,+}(\mathbf{q}_C) C_{a_1' a_2'}^{\text{RPA}}(\mathbf{q}_C), \\ &= \left[\{1 - C[\hat{\Gamma}^0] \hat{\chi}^0\}^{-1} C[\hat{\Gamma}^0] \right]_{a_3 a_4}(\mathbf{q}_C), \end{aligned} \quad (27)$$

where $\Gamma^0 = \hat{U}$ denotes the initial Hubbard interaction vertex written in the subspace of the spin-valley/orbital degrees of freedom.

B. RPA mechanism for superconductivity

From the effective RPA vertex $\hat{C}^{\text{RPA}}(\mathbf{q}_C)$ in the crossed particle-hole channel, we can construct an effective pairing vertex that accounts for the formation of (zero-momentum) Cooper pairs by virtue of spin fluctuation exchange. This

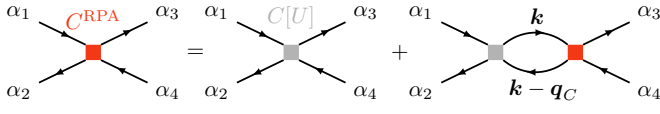


FIG. 13. Diagrams contributing to the single-channel RPA resummation in the crossed particle-hole channel including only Hubbard-type interaction \hat{U} .

requires we have not yet reached the critical interaction $\alpha_c \hat{U}$ given by the divergence of $C^{\text{RPA}}(\mathbf{q}_C)$ signaling the formation of an emergent exchange instability. Projecting the effective RPA vertex into the pairing channel yields

$$[\Gamma^P]_{a_3 a_4}^{a_1 a_2}(\mathbf{k}_P, \mathbf{k}'_P) = P[\Gamma^0]_{a_3 a_4}^{a_1 a_2}(\mathbf{k}_P, \mathbf{k}'_P) + C_{a_1 a_4}^{\text{RPA}}(\mathbf{k}_P + \mathbf{k}'_P) - C_{a_2 a_4}^{\text{RPA}}(\mathbf{k}_P - \mathbf{k}'_P), \quad (28)$$

where the last term ensures that the effective interaction tensor obeys fermionic anti-commutation relations. To analyze the symmetry of the leading superconducting order parameter, we then solve a linearized gap equation in spin/orbital space

$$\lambda_{\text{SC}} \Delta_{a_1 a_2}(\mathbf{k}_P) = \frac{1}{N_{\mathbf{k}'_P}} \sum_{\mathbf{k}'_P} \sum_{a'_1 a'_2} \sum_{a_3 a_4} [\Gamma^P]_{a_3 a_4}^{a_1 a_2}(\mathbf{k}_P, \mathbf{k}'_P) \chi_{a_3 a_4}^{0, -}(\mathbf{q}_P = 0, \mathbf{k}'_P) \Delta_{a'_1 a'_2}(\mathbf{k}'_P), \quad (29)$$

where the non-interacting particle-particle susceptibility is defined in Eq. (26).

-
- [1] F. Wu, T. Lovorn, E. Tutuc, I. Martin, and A. MacDonald, *Physical review letters* **122**, 086402 (2019).
[2] T. Devakul, V. Crépel, Y. Zhang, and L. Fu, *Nature communications* **12**, 6730 (2021).
[3] Y. Jia, J. Yu, J. Liu, J. Herzog-Arbeitman, Z. Qi, H. Pi, N. Regnault, H. Weng, B. A. Bernevig, and Q. Wu, *Physical Review B* **109**, 205121 (2024).
[4] T. Fukui, Y. Hatsugai, and H. Suzuki, *Journal of the Physical Society of Japan* **74**, 1674 (2005), <https://doi.org/10.1143/JPSJ.74.1674>.
[5] S. Carr, S. Fang, H. C. Po, A. Vishwanath, and E. Kaxiras, *Phys. Rev. Res.* **1**, 033072 (2019).
[6] A. Fischer, L. Klebl, D. M. Kennes, and T. O. Wehling, arXiv preprint arXiv:2407.02576 (2024).
[7] N. Marzari, A. A. Mostofi, J. R. Yates, I. Souza, and D. Vanderbilt, *Rev. Mod. Phys.* **84**, 1419 (2012).
[8] V. Crépel and A. Millis, *Physical Review Research* **6**, 033127 (2024).
[9] R. E. Throckmorton and O. Vafek, *Phys. Rev. B* **86**, 115447 (2012).
[10] M. Salmhofer and C. Honerkamp, *Progress of Theoretical Physics* **105**, 1 (2001), <https://academic.oup.com/ptp/article-pdf/105/1/1/5164880/105-1-1.pdf>.
[11] W. Metzner, M. Salmhofer, C. Honerkamp, V. Meden, and K. Schönhammer, *Rev. Mod. Phys.* **84**, 299 (2012).
[12] C. Platt, W. Hanke, and R. Thomale, *Advances in Physics* **62**, 453 (2013), <https://doi.org/10.1080/00018732.2013.862020>.
[13] N. Dupuis, L. Canet, A. Eichhorn, W. Metzner, J. Pawłowski, M. Tissier, and N. Wschebor, *Physics Reports* **910**, 1 (2021), the nonperturbative functional renormalization group and its applications.
[14] J. Beyer, J. B. Profe, and L. Klebl, *The European Physical Journal B* **95**, 65 (2022).
[15] C. Husemann and M. Salmhofer, *Phys. Rev. B* **79**, 195125 (2009).
[16] J. Lichtenstein, D. Sánchez de la Peña, D. Rohe, E. Di Napoli, C. Honerkamp, and S. Maier, *Computer Physics Communications* **213**, 100 (2017).
[17] J. B. Profe and D. M. Kennes, *The European Physical Journal B* **95**, 60 (2022).
[18] J. B. Profe, D. M. Kennes, and L. Klebl, *SciPost Phys. Codebases*, 26 (2024).
[19] A. Fischer, L. Klebl, J. B. Profe, A. Rothstein, L. Waldecker, B. Beschoten, T. O. Wehling, and D. M. Kennes, *Phys. Rev. Res.* **6**, L012003 (2024).